Comprehensive comparison of pore-scale models for multiphase flow in porous media

Zhao, B., MacMinn, C., Primkulov, B. K., Chen, Y., Valocchi, A. J., Zhao, J., Kang, Q., Bruning, K., McClure, J. E., Miller, C. T., Fakhari, A., Bolster, D., Hiller, T., Brinkmann, M., Cueto-Felgueroso, L., Cogswell, D. A., Verma, R., Prodanovic, M., Maes, J., Geiger, S. Vassvik, M., Hansen, A., Segre, E., Holtzman, R., Yang, Z, Yuan, C., Chareyre, B. & Juanes, R.

Comprehensive comparison of pore-scale models for multiphase flow in porous media

Benzhong Zhao,[1] Christopher W. MacMinn,[2] Bauyrzhan K. Primkulov,[3] Yu Chen,[4] Albert J. Valocchi,[4]
Jianlin Zhao,[5] Qinjun Kang,[6] Kelsey Bruning,[7] James E. McClure,[8] Cass T. Miller,[7] Abbas Fakhari,[9]
Diogo Bolster,[9] Thomas Hiller,[10] Martin Brinkmann,[11] Luis Cueto-Felgueroso,[12] Daniel A. Cogswell,[13]
Rahul Verma,[14] Maša Prodanović,[14] Julien Maes,[15] Sebastian Geiger,[15] Morten Vassvik,[16] Alex Hansen,[16]
Enrico Segre,[17] Ran Holtzman,[18] Zhibing Yang,[19] Chao Yuan,[20] Bruno Chareyre,[20] and Ruben Juanes[3, *]

[1]*McMaster University, Hamilton, ON, Canada*
[2]*University of Oxford, Oxford, UK*
[3]*Massachusetts Institute of Technology, Cambridge, MA, USA*
[4]*University of Illinois at Urbana-Champaign, Urbana, IL, USA*
[5]*Swiss Federal Institute of Technology in Zürich, Zürich, Switzerland*
[6]*Los Alamos National Laboratory, Los Alamos, NM, USA*
[7]*University of North Carolina at Chapel Hill, Chapel Hill, NC, USA*
[8]*Virginia Polytechnic Institute & State University, Blacksburg, VA, USA*
[9]*University of Notre Dame, Notre Dame, IN, USA*
[10]*Leibniz Institute for Applied Geophysics, Hannover, Germany*
[11]*Saarland University, Saarbrücken, Germany*
[12]*Universidad Politécnica de Madrid, Madrid, Spain*
[13]*Aramco Services Company: Aramco Research Center-Boston, Cambridge, MA, USA*
[14]*University of Texas at Austin, Austin, TX, USA*
[15]*Heriot-Watt University, Edinburgh, UK*
[16]*Norwegian University of Science and Technology, Trondheim, Norway*
[17]*Weizmann Institute of Science, Rehovot, Israel*
[18]*The Hebrew University of Jerusalem, Rehovot, Israel; Coventry University, Coventry, UK*
[19]*Wuhan University, Wuhan, China*
[20]*Grenoble Institute of Technology, Grenoble, France*
(Dated: May 23, 2019)

Multiphase flows in porous media are important in many natural and industrial processes. Pore-scale models for multiphase flows have seen rapid development in recent years, and are becoming increasingly useful as predictive tools in both academic and industrial applications. However, quantitative comparisons between different pore-scale models, and between these models and experimental data, are lacking. Here, we perform an objective comparison of a variety of state-of-the-art pore-scale models, including lattice Boltzmann, stochastic rotation dynamics, volume-of-fluid, level-set, phase-field, and pore-network models. As the basis for this comparison, we use a dataset from recent microfluidic experiments with precisely controlled pore geometry and wettability conditions, which offers an unprecedented benchmarking opportunity. We compare the results of the 14 participating teams both qualitatively and quantitatively using several standard metrics, such as fractal dimension, finger width, and displacement efficiency. We find that no single method excels across all conditions, and that thin films and corner flow present substantial modelling and computational challenges.

I. INTRODUCTION

Multiphase flows in porous media are central to a wide range of natural and industrial processes, including geologic CO_2 sequestration, enhanced oil recovery, and water infiltration into soil. Predictive modelling of these processes requires a clear understanding of the pore-scale mechanisms of fluid-fluid displacement. These pore-scale processes can be simulated using a variety of different approaches, including lattice/particle-based methods such as the lattice Boltzmann method, upscaled continuum methods such as phase-field models, and topological methods such as pore-network models [1]. All of these models must confront a variety of fundamental challenges related to resolving the combined effects of capillarity, wetting, and viscous instability within a

complex geometry, including thin films, moving contact lines, and the pinch-off and merging of interfaces. These mechanisms combine to produce macroscopic displacement patterns that are strongly dependent on the relative affinity of the solid for the different fluids (*i.e.*, wettability), the importance of viscous forces relative to capillary forces (*i.e.*, capillary number), and the pore geometry. As a result, pore-scale modelling of multiphase flow in porous media, even for relatively simple pore geometries, remains an open challenge and a very active area of research.

Historically, comparisons between pore-scale models and experimental data have been hampered by limitations on both fronts. The vast majority of existing experimental observations have been limited to macroscopic features and a narrow range of wettability conditions (strong drainage), and do not include a precise description of the associated pore geometry. In addition, most pore-scale models are very computationally expensive; only recently have these methods been able to simulate flow through a sufficiently large number of pores

---
* juanes@mit.edu

to reproduce macroscopic observables thanks to advances in both modelling methods and computing power. At the same time, modern experimental techniques now allow for high-resolution experimental observations and detailed characterization of pore geometry [1]. One recent dataset, in particular, provides high-resolution observations across a wide range of wettabilities and capillary numbers in a well-defined and relatively simple pore geometry [2]. These observations offer an unprecedented benchmarking opportunity for pore-scale models. The goal of this benchmark is to compare a wide variety of state-of-the-art pore-scale modelling approaches with experimental observations in terms of both pore-scale mechanisms and macroscopic displacement patterns.

II. RESULTS

A. Dataset

The benchmark study is based on the experiments of Zhao *et al.* [2] (Fig. 1). In the experiments, water was injected ($\eta_{\text{water}} = 0.99$ mPa · s) into a viscous silicone oil ($\eta_{\text{oil}} = 340$ mPa · s) in quasi-2D microfluidic flow cells patterned with vertical posts. This is a strongly viscously unstable displacement with viscosity ratio $\mathcal{M} = \eta_{\text{oil}}/\eta_{\text{water}} \approx 340$. The large unfavorable viscosity ratio of the experimental dataset was motivated by several considerations: it allows for direct comparison with previous wettability-related experimental studies [3, 4], it helps to highlight the impact of wettability on viscous instabilities, and it is directly relevant to applications like waterflooding of heavy crude oil [5].

The importance of viscous forces relative to capillary forces in the experiments was characterized using the classical capillary number Ca $= \eta_{\text{oil}}v_{\text{inj}}/\gamma$, where $\gamma = 13 \pm 2$mN/m is the interfacial tension between the fluids and $v_{\text{inj}} = Q/(bd)$ is the characteristic injection velocity as constrained by the gap thickness $b = 100$ μm and the median pore-throat size $d = 300$ μm. The experiments were conducted at three distinct values of Ca spanning two orders of magnitude: Ca $= 0.029$ ("low Ca"), 0.29 ("intermediate Ca"), and 2.9 ("high Ca").[1] Note that these values of Ca provide a nominal macroscopic characterisation of the flow, but the actual strength of viscous to capillary forces varies locally due pore-scale heterogeneity, preferential pathways, and the radial flow geometry. Note also that the lowest value of Ca considered here is still moderate relative to a truly quasi-static displacement. The wettability of the flow cell was characterized using the static advancing contact angle θ of water immersed in silicone oil. The experiments were conducted at five distinct values of θ spanning the full range of wettability conditions: $\theta = 150°$ ("strong drainage"), $120°$ ("weak drainage"), $90°$ ("neutral"), $60°$ ("weak imbibition"), and $7°$ ("strong imbibition"). The participating teams were given the exact geometry of the post

pattern and, for each experimental condition, a series of data files describing the time evolution of the gap-averaged water saturation S at high spatial resolution. To allow for qualitative and quantitative comparisons between methods without imposing an excessive computational burden on participants, we identified four "priority cases" that best represent the diversity of patterns and physical mechanisms that emerge from fluid-fluid displacement under different Ca and wettability conditions:

1. Strong drainage at high Ca (SD-HC): Canonical viscous fingering pattern with incomplete pore-scale displacement due to formation of trailing films of the defending fluid.

2. Weak imbibition at low Ca (WI-LC): Compact displacement pattern due to cooperative pore filling.

3. Strong imbibition at intermediate Ca (SI-IC): Thin-film flow of the invading fluid along the top and bottom walls, accompanied by a ramified fingering pattern formed by corner flow.

4. Strong imbibition at low Ca (SI-LC): Corner-flow-driven "chaining" of posts.

B. Participating teams and methods

A total of 14 teams contributed modelling results to the benchmark study (Table I). Together, they applied many different pore-scale modelling methods (Table I and *SI Appendix* Note 1). The methods can be categorized into three major classes: lattice/particle-based models, continuum models, and pore-network models. Lattice/particle-based models simulate the motion and interaction of a large number of microscopic particles that collectively give rise to macroscopic behavior satisfying the relevant continuum equations (e.g., Navier-Stokes). The fluid-fluid interface is captured implicitly as the boundary between the multi-colored particles that represent the different fluid phases. These models include the lattice Boltzmann (LB) methods [6] and stochastic rotation dynamics (SR) models [7]. Continuum models solve macroscopic equations for fluid flow while tracking the interface implicitly via the evolution of an indicator variable. These models include volume-of-fluid (VF) methods [8], level-set (LS) methods [9], and phase-field (PF) models [10]. Pore-network (PN) models simulate fluid flow through an idealized network of pores connected by throats [11]. The macroscopic interface is represented explicitly as the boundary between invaded and non-invaded pores. It speaks to the physical complexity of this problem that only one of the contributions (VF1) attempted direct simulation of the Navier-Stokes (or Stokes) equations with evolving fluid-fluid interfaces. Note also that only LB1, LB3, and SR1 conducted truly 3D simulations.

C. Qualitative performance measures

The interplay between wettability and Ca generates a wide spectrum of 2D displacement patterns that range from rami-

---

[1] Note that the Ca values reported in [2] are incorrect—They are too small by one order of magnitude.
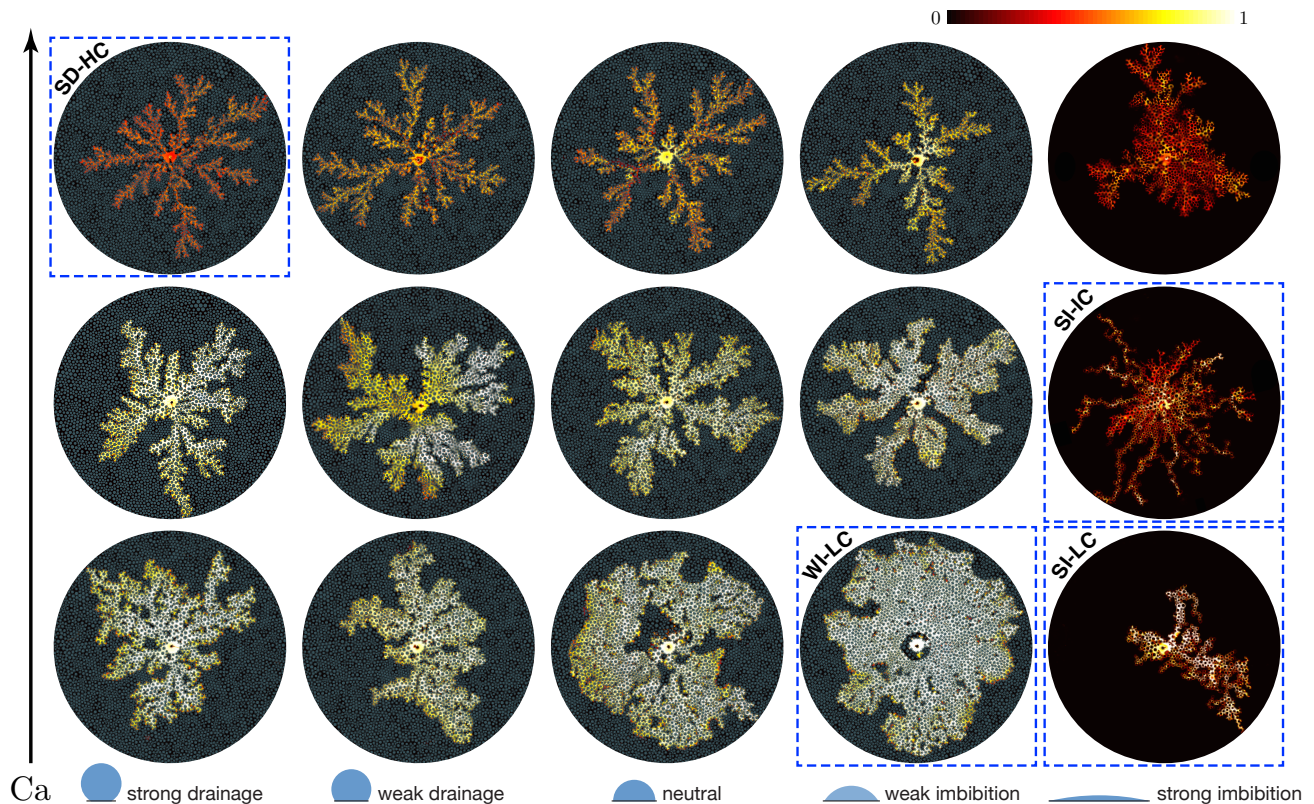
FIG. 1: Experimental phase diagram showing the displacement pattern at breakthrough for different wettability conditions (left to right: $\theta = 150°$, $120°$, $90°$, $60°$, $7°$) and capillary numbers (bottom to top: Ca = 0.029, 0.29, 2.9). The colormap shows the gap-averaged saturation of the invading fluid. The four "priority cases" for the benchmark study are outlined in dashed blue: Strong drainage at high Ca (SD-HC), weak imbibition at low Ca (WI-LC), strong imbibition at intermediate Ca (SI-IC), and strong imbibition at low Ca (SI-LC). *Adapted from [2].*

fied fingers to compact fronts (Fig. 1). Additional 3D information is provided by the local gap-averaged saturation of the invading fluid (Fig. 1). The displacement pattern and saturation distribution at the end of the simulation, when the invading fluid reaches the outer edge of the computational domain, serve as a good basis for qualitative and quantitative comparisons (e.g., Fig. 3 & *SI Appendix*).

D. Quantitative performance measures

For quantitative comparison, we calculate four performance measures from the displacement pattern at the end of each simulation, when the invading fluid reaches the outer edge of the domain:

1. Fractal dimension D_f, as calculated via the box-counting method. This is a classical measure of the degree to which a pattern fills space in 2D [40].

2. Average dimensionless finger width W_f, as measured at half the radius of the computational domain and scaled by the median post diameter. Note that this measure is very sensitive to domain size for compact displacements, and that not all groups used the same domain

size.

3. Gap-averaged saturation S of the invading fluid, as represented by its median value as well as the first and third quartiles. Note that many methods ignore films and therefore assume $S = 1$ in invaded regions.

4. Displacement efficiency E_d, which is the fraction of the defending fluid that has been displaced from the domain.

Details on how we calculated the quantitative performance measures can be found in *SI Appendix* Note 2.

E. Submission of simulation results

While some teams submitted results for many of the conditions in the experimental phase diagram (Fig. 1), most teams only contributed results for a relevant subset of the priority cases (Table I, *SI Appendix*). For example, some methods were developed for quasi-static displacement (*i.e.*, small Ca; LS1, PN5), and therefore could not be applied to intermediate or high Ca conditions. Other methods were developed for drainage only (PN4, PN5), and therefore could not be applied to imbibition scenarios. Additionally, some teams simulated a

Label	Authors	Method	Dim.	Comp. Dom.	Res.	$\mathcal{M}$	Remarks	Refs.
LB1	Y. Chen, A. Valocchi	Lattice Boltzmann	3	50%, 80%	14.3	5, 40, 100	Artificial precursor film in strong imbibition.	[12, 13]
LB2	J. Zhao, Q. Kang	Lattice Boltzmann	2	100%	20.2	340	Perturbation & recoloring operators generate interfacial tension & phase segregation, respectively.	[14, 15]
LB3	K. Bruning, J. McClure, C. Miller	Lattice Boltzmann	3	40%	13	100	Increased domain thickness to 448 μm to better resolve film formation in the gap.	[16, 17]
LB4	A. Fakhari, D. Bolster	Lattice Boltzmann	2	100%	~ 100	340	LB equation based on the conservative phase-field method.	[18, 19]
SR1	T. Hiller, M. Brinkmann	Stochastic rotation dynamics	3	60%	~ 300	1–5	Limited resolution in the gap, leading to unrepresentative saturation.	[20, 21]
PF1	L. Cueto-Felgueroso	Phase field	2	100%	~ 30	340	Diffuse interface model that captures 3D physics.	[22, 23]
PF2	D. Cogswell	Phase field	2	100%	~ 50	340	Variational boundary condition sets the contact angle.	[24]
LS1	R. Verma, M. Prodanovic	Level set	2	100%	24.9	n.a.	Quasi-static; simulates trapped fluid via immobile "masks".	[25–28]
VF1	J. Maes, S. Geiger	Volume-of-fluid	2	100%, 60%	~ 80	340	Implemented in OpenFOAM as an internal VOF solver (*interFoam*).	[29, 30]
PN1	M. Vassvik, A. Hansen	Pore network	2	100%	n.a.	340	Single pressure, dynamic model; ignores the out-of-plane curvature.	[31, 32]
PN2	E. Segre, R. Holtzman	Pore network	2	100%	n.a.	340	Single pressure, dynamic model; ignores the out-of-plane curvature.	[33, 34]
PN3	B. Primkulov, B. Zhao, C. W. MacMinn, R. Juanes	Pore network	2	100%	n.a.	340	Single pressure, dynamic model; includes the out-of-plane curvature; quasi-static version of the model captures corner flow.	[35, 36]
PN4	Z. Yang	Pore network	2	100%	n.a.	340	Single pressure, dynamic model; includes the out-of-plane curvature.	[37]
PN5	C. Yuan, B. Chareyre	Pore network	2	100%	n.a.	n.a.	Quasi-static model for strong drainage; includes the out-of-plane curvature.	[38, 39]

TABLE I: Summary of contributions. See *SI Appendix* Note 3–5 for further details on methods. Dim.: Dimensionality. Comp. Dom.: Radius of computational domain as a percentage of the radius of the experimental domain. Res.: Resolution of the computational domain in μm per grid block/lattice.
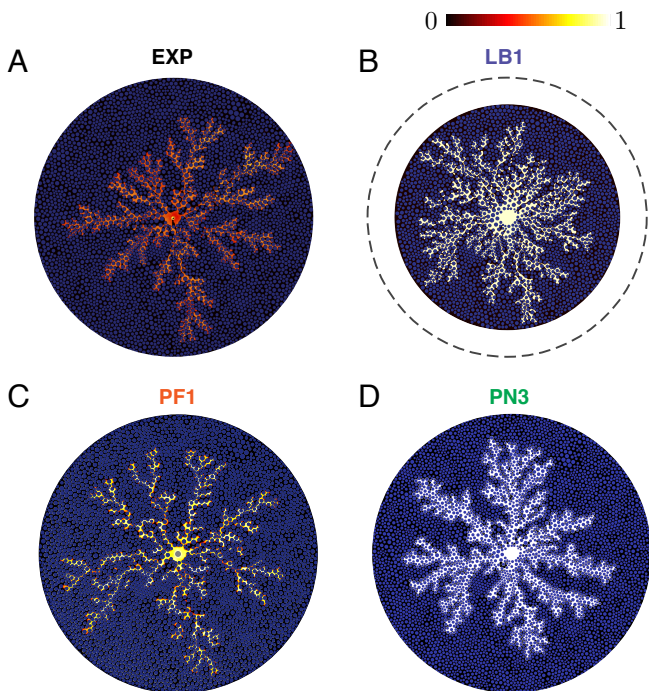
FIG. 2: Comparison between (A) the experimental displacement pattern and (B–D) selected simulated displacement patterns for the case of strong drainage at high Ca (SD-HC). The simulations capture the slender, ramified fingering patterns of SD-HC well, though they are produced by three distinctly different classes of modeling methods. The three methods differ most strongly in how well they reproduce the residual wetting films, as illustrated by the colormap.
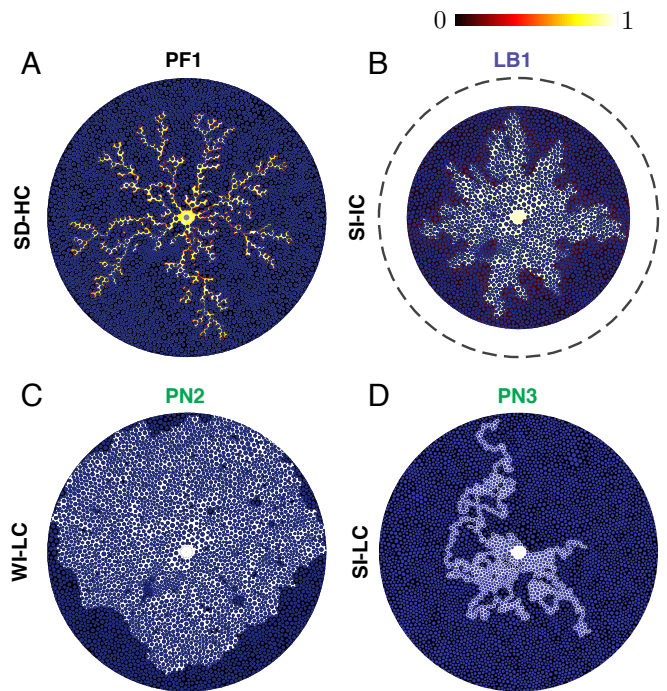
FIG. 3: Selection of simulated displacement patterns for the priority cases. (A) Strong drainage at high Ca (SD-HC) as simulated by a phase-field model. (B) Strong imbibition at intermediate Ca (SI-IC) as simulated by a lattice Boltzmann model at a reduced viscosity ratio ($\mathcal{M} = 40$). (C) Weak imbibition at low Ca (WI-LC) as simulated by a pore-network model. (D) Strong imbibition at low Ca (SI-LC) as simulated by a pore-network model.

subset of the experimental domain (*i.e.* truncated at a smaller outer radius; LB1, LB3, SR1, VF1) due to computational constraints.

F. Performance of the methods

SD-HC: The experimental displacement pattern for SD-HC displays classical viscous fingering, known for the slender, ramified fingers mimicked by diffusion-limited aggregation (Fig. 1) [41, 42]. Remarkably, all three classes of methods are able to capture these patterns (Fig. *S1*). Quantitative analysis of the simulated patterns reveals that while most methods reproduce W_{f} to within a factor of 60%, most methods overpredict D_f, and all methods overpredict E_{d}, often by several-fold (Fig. *4A*). The latter discrepancy is a consequence of incomplete pore-scale displacement due to the well-known formation of thin trailing films of the defending fluid at high Ca [43, 44]. Most methods ignore these films, and those that capture them tend to under-predict their thickness, which corresponds to over-predicting S (Fig. *4A*). The PF methods appear to do a reasonable job of capturing this incomplete displacement without simulating the full 3D problem. Note that LB1, LB3, SR1, and VF1 simulate a subset of the full domain,

and that LB1, LB3, and SR1 simulate at a reduced $\mathcal{M}$. Displacement at high Ca is very sensitive to viscosity ratio, and the predictions of the latter methods are affected accordingly.

WI-LC: The experimental displacement pattern for WI-LC shows compact displacement as a result of cooperative pore filling [33, 45]. Qualitatively, all three classes of methods are again able to capture these patterns (Fig. *S2*). Most methods capture D_f to within a few percent, suggesting that the methods reproduce the 2D features of the pattern (Fig. *4B*). This case does not feature thin films, so S is nearly 1; as a result, those methods that capture D_f well also capture E_{d}. Note that LB1, SR1, and VF1 simulate a subset of the full domain, and LB1 and SR1 simulate at a reduced $\mathcal{M}$. Displacement at low Ca is not very sensitive to viscosity ratio, so the latter two methods still perform well in this scenario.

SI-IC: The experimental displacement pattern for SI-IC shows a highly ramified, yet roughly axisymmetric fingering pattern, the backbone of which is formed by the successive "chaining" of posts by preferential flow along the post-wall corners [2]. The resulting pattern has low values of S because the strongly wetting invading fluid propagates primarily by corner flow and in thin films along the top and bottom walls, bypassing pore bodies [2, 46, 47]. Qualitatively, none of the methods reproduce the ramified backbone of linked posts (Fig. *S3*). Most methods fail to capture the emergence
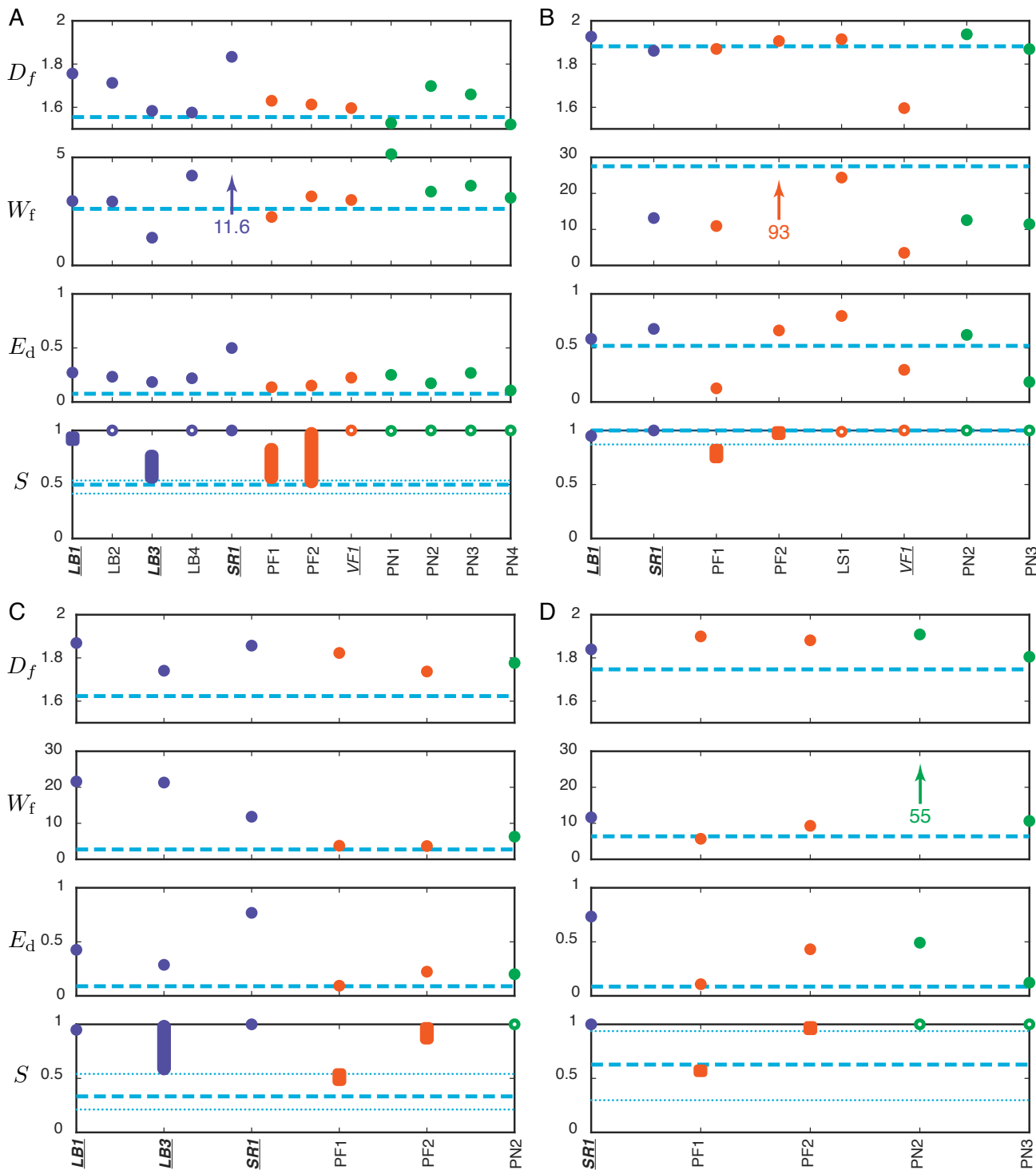
FIG. 4: Quantitative performance results for (A) SD-HC, (B) WI-LC, (C) SI-IC, and (D) SI-LC. First row: Fractal dimension D_f. Second row: Average dimensionless finger width W_f. Third row: Displacement efficiency E_d. Fourth row: Gap-averaged saturation S of the invading fluid in invaded regions, with symbols spanning the range from first quartile to third quartile. In the latter, open circles indicate methods that neglect films and therefore assume $S = 1$ in invaded regions. In all cases, we also plot the corresponding experimental measurement (dashed blue line); for S, we show the first and third quartiles (dotted blue lines) in addition to the median value. *Italic labels* on the horizontal axis denote contributions that simulate a subset of the experimental domain, while **bold labels** denote contributions that simulate at a reduced $\mathcal{M}$ relative to the experiments.

of corner flow, typically overestimating W_f and greatly over-

estimating E_d (Fig. 4C). Fully 3D methods should be able to

capture corner flow and film flow, and images from the 3D simulations (LB1, LB3, SR1) suggest that they do, at least to some extent (Fig. 5). However, because of the high computational demands, all three of these methods simulate subsets of the full domain at greatly reduced $\mathcal{M}$; the latter suppresses the strong preferential flow through thin films that should occur for large $\mathcal{M}$. Quasi-3D (gap-averaged) phase-field methods (PF1, PF2) can capture film flow through their upscaled representation of the affinity of the invading fluid for both the walls and the posts, but cannot capture corner flow without an explicit sub-model for the presence of corners. Pore-network models would require explicit sub-models for both film flow and corner flow.

SI-LC: The experimental displacement pattern for SI-LC is completely controlled by nearly quasi-static invasion through corner flow. Corner films link groups of posts via bursts, and then surrounded pores fill slowly and almost completely. Unlike SI-IC, these patterns have a relatively large value of S and no axial symmetry or well-defined fingers or branches. Relatively few participants attempted this case because it involves both low Ca (computationally demanding for 3D methods) and corner flow (absent from most methods). Qualitatively, the simulation results are quite variable (Fig. *S4*). PN3 captures post-chaining via corner flow with a dedicated sub-model for corner flow, but does not capture the subsequent filling-in (Fig 3); PF1 captures the rough shape, but without clear post-chains. Quantitatively, all methods over-predict D_f, but all methods are relatively close to the experimental value (Fig. *4D*). All methods except for PF1 also over-predict W_f by a factor of 2 or more. Only PF1 and PF2 are able to make quantitative predictions of S (SR1, PN2, and PN3 assume $S = 1$); PF1 reproduces the experimental value of S very closely, whereas PF2 significantly over-predicts S. PF1 and PN3 both capture E_d relatively well; PF1 is arguably the best match overall.

G. Thin films and corner flow

The complex nature of interfacial flows in the presence of solid surfaces lends an inherently 3D nature to fluid-fluid displacement processes, even in quasi-1D geometries such as capillary tubes [48] and quasi-2D geometries such as Hele-Shaw cells [46]. In a patterned micromodel, these 3D effects include the propagation of thin films along the top and bottom walls and the surfaces of the posts, and in the corners where the walls and posts meet [2, 47]. While both fully 3D methods (LB1, LB3) and quasi-3D (gap-averaged) methods (PF1, PF2) predict the formation of trailing films in SD-HC, only fully 3D methods (LB1, LB3) capture films in SI-IC. The color-gradient wetting model used in LB1 leads to an artificial film ($\sim 14\,\mu$m) that slowly permeates the entire simulation domain. This film accumulates on the posts to form corner films and pendular rings that resemble those observed in the experiments (Fig. *5B*). However, this film also uniformly coats the top and bottom walls, and the resulting mass transport appears to suppress the strong preferential flows observed in the experiment. LB3 uses a similar wetting model, and should
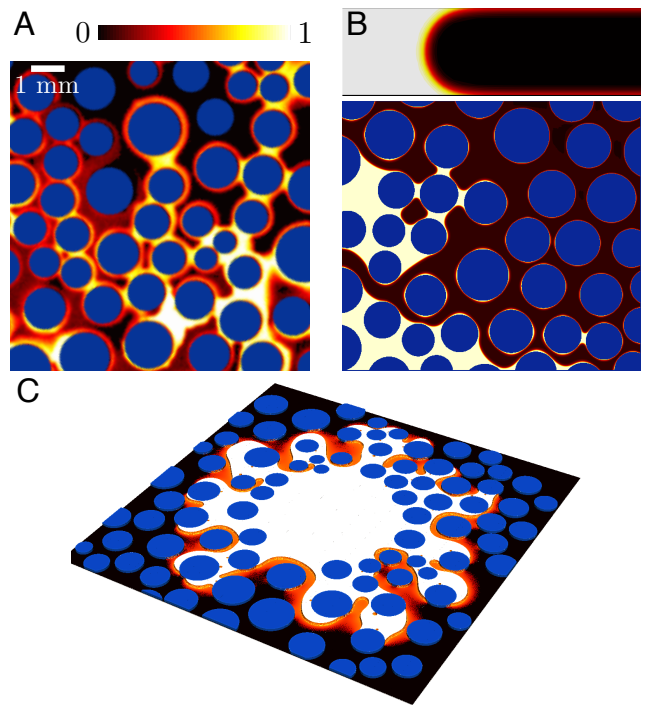

FIG. 5: (A) Experimental snapshot of SI-IC at the pore scale, which is characterized by the co-existence of thin films and corner flow. (B) Simulation results of LB1 for SI-IC ($\mathcal{M} = 40$). Top: Cross-sectional view showing the leading thin films along the top and bottom walls. Bottom: Plan view showing the co-existence of thin films and corner flow, as well as pendular rings that link neighboring posts. (C) Isometric projection of the 3D simulation results of LB3 for SI-IC ($\mathcal{M} = 100$), showing the propagation of thin films ahead of the main invasion front.

therefore have the same feature (Fig. 5*C*). Both of these methods are very computationally demanding due to the very large number of particles needed to resolve a 3D flow. For a given scenario, the computational cost also scales with the number of timesteps and the timestep size. The timestep size is constrained by $\mathcal{M}$ for numerical stability, whereas the number of timesteps to breakthrough scales with the domain size. As a result, LB1 and LB3 simulate a subset of the full domain, and at a reduced $\mathcal{M}$.

III. DISCUSSION

The goal of this benchmark study was to assess the degree to which different state-of-the-art modeling strategies could reproduce the correct macroscopic features (and some pore-scale features) of fluid–fluid displacement in a porous medium under different wetting conditions. These pore-scale models have become widely-used tools in extracting macroscopic properties of geologic porous media (*e.g.*, relative permeability) [49–52], and in designing synthetic porous materials with desirable transport properties in electrochemical de-

vices [53, 54]. In all these cases, the accuracy of the model output hinges upon its ability to correctly account for the impact of wettability at different capillary numbers.

Most methods were able to capture viscous instability and fingering at high flow rates (IC and HC), and most were also able to capture the more subtle broadening of features in WI where the low contact angle enables cooperative pore filling. In contrast, few methods were able to capture the thin trailing films that form for SD-HC, the thin leading films that occur for SI-IC, and the corner films that dominate SI-LC, all of which are inherently 3D.

For 2D models, films present a modelling challenge. Gap-averaged PF models were able to capture trailing films in SD-HC, although leading films in SI-IC and corner flow in SI-LC remain elusive. Other 2D models were unable to capture films to any noteworthy extent. PN3 was the only model to explicitly account for corner flow, and was reasonably successful in doing so for quasi-static displacement. However, extending such a model to include viscous effects and residual films is nontrivial because many of the underlying physical phenomena, such as flow through corner networks, film bridging from post to post, and post-chaining avalanches, are poorly understood.

For 3D models, films present a serious computational challenge. Resolving films is nontrivial due to the large aspect ratio of the problem—the flow cell has a radius of 100 mm, the gap thickness is 100 μm, and the film thickness ranges from tens of microns to a few microns or less. LB1, LB2, and LB3 addressed this challenge most directly, running 3D simulations with $\sim$160 million, $\sim$160 million, and $\sim$300 million lattice sites, respectively. Even after reducing the viscosity ratio and truncating the domain in order to relax time-step restrictions, these simulations required world-class computational resources. Despite this substantial effort, these simulations could only achieve a spatial resolution of 10–20 μm, which is barely small enough to allow for films and certainly not small enough to resolve them. All three groups agree that this problem pushes the limits of what is currently possible. More importantly, these simulations showed both qualitatively and quantitatively that failure to resolve films at the small-scale can have important consequences for the *macroscopic flow pattern*.

It is well-known that pre-existing wetting films are common in subsurface applications such as enhanced oil recovery, and that their presence has a significant impact on the macroscopic transport properties such as relative permeability [55, 56]. These pre-existing films would be an active, evolving component of the displacement as they swell, disconnect, reconnect, and pinch-off—particularly in partial wetting conditions. Resolving them (and the flow within them) would be an essential and challenging part of the problem.

This benchmark targets the "many-pore" scale (hundreds to thousands of pores), as this is a scale large enough to manifest the collective dynamics characteristic of fluid–fluid displacements in porous media (viscous fingering, capillary fingering, avalanches, etc.), and small enough that computational models are routinely used to make predictions. Thus, it is natural to ask whether those predictions are accurate. There is,

however, an underlying scale at which "single-pore" fluid-mechanics details emerge (such as menisci deformation and merging, contact-line pinning and motion, contact-angle hysteresis, post wetting dynamics, etc). The inclusion of these effects will further increase the computational complexity of the problem, which makes it impractical at the scale of hundreds to thousands of pores considered in the current study, and comparison of different methods at this single-pore scale would require an altogether different type of benchmark study in a simpler geometry (*e.g.*, Verma *et al.*, 2018 [27]). Furthermore, real rocks such as carbonates also have a wider pore size distribution than the one from our micromodel [57], a feature that would likely have an effect on the correlation between pore occupancy and pore size that is absent from our experimental benchmark.

A key contribution of this benchmark is to demonstrate the capabilities and limitations of three major classes of pore-scale models (*i.e.*, lattice/particle-based models, continuum models, and pore-network models) in predicting the macroscopic features of unstable two-phase flows in the presence of solid surfaces. We find that all three classes of models are capable of predicting the transition from strong drainage to weak imbibition. Specifically, pore-network models offer superior computational efficiency, but they lack the ability to resolve gap-averaged saturations that the more computationally intensive lattice/particle-based models and continuum models offer. Only 3D lattice/particle-based models could simulate leading films and corner flow in strong imbibition, but their spatial and temporal resolutions are severely limited by the prohibitive computational demand. Our results highlight the need for further effort along multiple complementary avenues in what is already a very active area of research.

The simulated displacement patterns for all priority cases are presented in *SI Appendix*, Figs. S1–S4. Details on how we calculated the quantitative performance measures of the priority cases can be found in *SI Appendix* Note 2. Descriptions of all the models, including their derivation and numerical implementation, are included in *SI Appendix* Note 3–5.

[1] M. J. Blunt, B. Bijeljic, H. Dong, O. Gharbi, S. Iglauer, P. Mostaghimi, A. Paluszny, and C. Pentland. Pore-scale imaging and modelling. *Adv. Water Resour.*, 51:197–216, 2013.

[2] B. Zhao, C. W. MacMinn, and R. Juanes. Wettability control on multiphase flow in patterned microfluidics. *Proc. Natl. Acad. Sci. USA*, 113(37):10251–10256, 2016.

[3] J. P. Stokes, D. A. Weitz, J. P. Gollub, A. Dougherty, M. O. Robbins, P. M. Chaikin, and H. M. Lindsay. Interfacial stability of immiscible displacement in a porous medium. *Phys. Rev. Lett.*, 57:1718–1721, 1986.

[4] M. Trojer, M. L. Szulczewski, and R. Juanes. Stabilizing fluid-fluid displacements in porous media through wettability alteration. *Phys. Rev. Applied*, 3:054008, 2015.

[5] J. M. Al-Besharah, O. A. Salman, and S. A. Akashah. Viscosity of crude oil blends. *Ind. Eng. Chem. Res.*, 26:2445–2449, 1987.

[6] S. Chen and G. D. Doolen. Lattice Boltzmann method for fluid flows. *Annu. Rev. Fluid Mech.*, 30:329–364, 1998.

[7] T. Ihle and D. M. Kroll. Stochastic rotation dynamics: A Galilean-invariant mesoscopic model for fluid flow. *Phys. Rev. E*, 63:020201, 2001.

[8] C. W. Hirt and B. D. Nichols. Volume of fluid (VOF) method for the dynamics of free boundaries. *J. Comput. Phys.*, 39:201–225, 1981.

[9] J. A. Sethian and P. Smereka. Level set methods for fluid interfaces. *Annu. Rev. Fluid Mech.*, 35:341–372, 2003.

[10] V. E. Badalassi, H. D. Ceniceros, and S. Banerjee. Computation of multiphase systems with phase field models. *J. Comput. Phys.*, 190:371–397, 2003.

[11] M. J. Blunt. Flow in porous media — pore-network models and multiphase flow. *Curr. Opin. Colloid Interface Sci.*, 6(197–207), 2001.

[12] Y. Chen, Y. Li, A. J. Valocchi, and K. T. Christensen. Lattice Boltzmann simulations of liquid CO_2 displacing water in a 2D heterogeneous micromodel at reservoir pressure conditions. *J. Contam. Hydrol.*, 212(14–27), 2018.

[13] J. Zhao, J. Yao, A. Li, M. Zhang, L. Zhang, Y. Yang, and H. Sun. Simulation of microscale gas flow in heterogeneous porous media based on the lattice Boltzmann method. *J. Appl. Phys.*, 120:084306, 2016.

[14] H. Liu, A. J. Valocchi, and Q. Kang. Three-dimensional lattice Boltzmann model for immiscible two-phase flow simulations. *Phys. Rev. E*, 85(4):046309, 2012.

[15] H. Liu, A. J. Valocchi, C. Werth, Q. Kang, and M. Oostrom. Pore-scale simulation of liquid CO_2 displacement of water using a two-phase lattice Boltzmann model. *Adv. Water Resour.*, 73:144–158, 2014.

[16] J. E. McClure, J. F. Prins, and C. T. Miller. A novel heterogeneous algorithm to simulate multiphase flow in porous media on multicore CPU-GUP systems. *Comput. Phys. Commun.*, 185:1865–1874, 2014.

[17] J. E. McClure, M. A. Berrill, W. G. Gray, and C. T. Miller. Tracking interface and common curve dynamics for two-fluid-phase flow in porous media. *J. Fluid Mech.*, 796:211–232, 2016.

[18] A. Fakhari and D. Bolster. Diffuse interface modeling of three-phase contact line dynamics on curved boundaries: A lattice Boltzmann model for large density and viscosity ratios. *J. Comput. Phys.*, 334:620–638, 2017.

[19] A. Fakhari, Y. Li, D. Bolster, and K. T. Christensen. A phase-field lattice Boltzmann model for simulating multiphase flows in porous media: Application and comparison to experiments of CO_2 sequestration at pore scale. *Adv. Water Resour.*, 114(119–134), 2018.

[20] T. Hiller, M. S. De La Lama, and M. Brinkmann. Stochastic rotation dynamics of wetting multi-phase flows. *J. Comput. Phys.*, 315:554–576, 2016.

[21] M. Jung, M. Brinkmann, R. Seemann, T. Hiller, M. S. De La Lama, and S. Herminghaus. Wettability controls slow immiscible displacement through local interface instabilities. *Phys. Rev. Fluids*, 1:074202, 2016.

[22] L. Cueto-Felgueroso and R. Juanes. A phase-field model of two-phase Hele-Shaw flow. *J. Fluid Mech.*, 758:522–552, 2014.

[23] L. Cueto-Felgueroso and R. Juanes. Macroscopic phase-field model of partial wetting: Bubbles in a capillary tube. *Phys. Rev. Lett.*, 108:144502, 2012.

[24] D. A. Cogswell and M. L. Szulczewski. Simulation of incompressible two-phase flow in porous media with large timesteps. *J. Comput. Phys.*, 345:856–865, 2017.

[25] M. Prodanović and S.L. Bryant. A level set method for determining critical curvatures for drainage and imbibition. *J. Colloid Interface Sci.*, 304(2):442–458, December 2006.

[26] E. Jettestuen, J. O. Helland, and M. Prodanović. A level set method for simulating capillary-controlled displacements at the pore scale with nonzero contact angles. *Water Resour. Res.*, 49:4645–4661, 2013.

[27] R. Verma, M. Icardi, and M. Prodanović. Effect of wettability on two-phase quasi-static displacement: Validation of two pore scale modeling approaches. *J. Contam. Hydrol.*, 212:115–133, 2018.

[28] R. Verma. *Pore scale modeling of multiphase flow in heterogeneously wet media*. PhD Thesis, The University of Texas at Austin, Austin, TX, USA, October 2018.

[29] S. Pavuluri, Maes. J., and F. Doster. Spontaneous imbibition in a microchannel: analytical solution and assessment of volume of fluid formulations. *Microfluidic Nanofluidic*, (22:90), 2018.

[30] J. Maes and S. Geiger. Direct pore-scale reactive transport modelling of dynamic wettability changes induced by surface complexation. *Adv. Water Resour*, 111:6–19, 2018.

[31] E. Aker, K. J. Måløy, A. Hansen, and G. G. Batrouni. A two-dimensional network simulator for two-phase flow in porous media. *Transp. Porous Med.*, 32:163–186, 1998.

[32] H. A. Knudsen, E. Aker, and A. Hansen. Bulk flow regimes and fractional flow in 2D porous media by numerical simulations. *Transp. Porous Med.*, 47:99–121, 2002.

[33] R. Holtzman and E. Segre. Wettability stabilizes fluid invasion into porous media via nonlocal, cooperative pore filling. *Phys. Rev. Lett.*, 115:164501, 2015.

[34] R. Holtzman. Effects of pore-scale disorder on fluid displacement in partially-wettable porous media. *Sci. Rep.*, 6(36221), 2016.

[35] B. K. Primkulov, S. Talman, K. Khalegh, A. R. Shokri, R. Chalaturnyk, B. Zhao, C. W. MacMinn, and R. Juanes. Quasi-static

fluid-fluid displacement in porous media: Invasion-percolation through a wetting transition. *Phys. Rev. Fluids*, 3:104001, 2018.

[36] B. K. Primkulov, A. A. Pahlavan, X. Fu, B. Zhao, C. W. MacMinn, and R. Juanes. Signatures of fluid-fluid displacement in porous media: Wettability, invasion events, patterns, and pressures. *Submitted for publication*.

[37] Z. Yang, A. Niemi, F. Fagerlund, and T. Illangasekare. Two-phase flow in rough-walled fractures: Comparison of continuum and invasion-percolation models. *Water Resour. Res.*, 49:993–1002, 2013.

[38] C. Yuan, B. Chareyre, and F. Darve. Pore-scale simulations of drainage in granular materials: finite size effects and the representative elementary volume. *Adv. Water Resour.*, 97:109–124, 2016.

[39] C. Yuan and B. Chareyre. A pore-scale method for hydromechanical coupling in deformable granular media. *Comput. Methods Appl. Mech Eng.*, 318:1066–1079, 2017.

[40] M. R. Schroeder. *Fractals, Chaos, Power Laws: Minutes from an Infinite Paradise*. W. H. Freeman and Company, Dover edition, 2009.

[41] L. Paterson. Diffusion-limited aggregation and two-fluid displacements in porous media. *Phys. Rev. Lett.*, 52(18):1621–1624, 1984.

[42] K. J. Måløy, J. Feder, and T. Jøssang. Viscous fingering fractals in porous media. *Phys. Rev. Lett.*, 55:2688–2691, 1985.

[43] G. I. Taylor. Deposition of a viscous fluid on the wall of a tube. *Journal of Fluid Mechanics*, 10(2):161–165, 1961.

[44] F. P. Bretherton. The motion of long bubbles in tubes. *Journal of Fluid Mechanics*, 10(2):166–188, 1961.

[45] M. Cieplak and M. O. Robbins. Influence of contact angle on quasistatic fluid invasion of porous media. *Phys. Rev. B*, 41(16):11508–11521, 1990.

[46] B. Levaché and D. Bartolo. Revisiting the Saffman-Taylor experiment: Imbibition patterns and liquid-entrainment transitions. *Phys. Rev. Lett.*, 113:044501, 2014.

[47] C. Odier, B. Levaché, E. Santanach-Carreras, and D. Bartolo. Forced imbibition in porous media: A fourfold scenario. *Phys. Rev. Lett.*, 119:208005, 2017.

[48] B. Zhao, A. A. Pahlavan, L. Cueto-Felgueroso, and R. Juanes. Forced wetting transition and bubble pinch-off in a capillary tube. *Phys. Rev. Lett.*, 120:084501, 2018.

[49] P. C. Reeves and M. A. Celia. A functional relationship between capillary pressure, saturation, and interfacial area as revealed by a pore-scale network model. *Water Resour. Res.*, 32(8):2345–2358, 1996.

[50] H. Rajaram, L. A. Ferrand, and M. A. Celia. Prediction of relative permeabilities for unconsolidated soils using pore-scale network models. *Water Resour. Res.*, 33(1):43–52, 1997.

[51] P. H. Valvatne and M. J. Blunt. Predictive pore-scale modeling of two-phase flow in mixed wet media. *Water Resour. Res.*, 40:W07406, 2004.

[52] L. Hao and P. Cheng. Pore-scale simulations on relative permeabilities of porous media by lattice Boltzmann method. *Int. J. Heat Mass Transf.*, 53:1908–1913, 2010.

[53] P. P. Mukherjee, Q. Kang, and C. Y. Wang. Pore-scale modeling of two-phase transport in polymer electrolyte fuel cells – progress and perspective. *Energy Environ. Sci.*, 4:346–369, 2011.

[54] F. Arbabi, H. Montazeri, R. Abouatallah, R. Wang, and A. Bazylak. Three dimensional computational fluid dynamics modelling of oxygen bubble transport in polymer electrolyte membrane electrolyzer porous transport layers. *J. Electrochem. Soc.*, 163(11):F3062–F3069, 2016.

[55] M. Blunt, M. J. King, and H. Scher. Simulation and theory of two-phase flow in porous media. *Phys. Rev. A*, 46(12):7680–7699, 1992.

[56] M.-H. Hui and M. Blunt. Effects of wettability on three-phase flow in porous media. *J. Phys. Chem. B*, 104:3833–3845, 2000.

[57] M. J. Blunt. *Multiphase flow in permeable media: A pore-scale perspective*. Cambridge University Press, 2017.

[58] A. K. Gunstensen, D. H. Rothman, S. Zaleski, and G. Zanetti. Lattice Boltzmann model of immiscible fluids. *Phys. Rev. A*, 43(8):4320–4327, 1991.

[59] P. Lallemand and L.S. Luo. Theory of the lattice Boltzmann method: Dispersion, dissipation, isotropy, Galilean invariance, and stability. *Phys. Rev. E*, 61(6):6546–6562, 2000.

[60] J. Tölke, S. Freudiger, and M. Krafczyk. An adaptive scheme using hierarchical grids for lattice Boltzmann multi-phase flow simulations. *Comput. Fluids*, 35(8–9):820–830, 2006.

[61] M. Latva-Kokko and D. H. Rothman. Static contact angle in lattice Boltzmann models of immiscible fluids. *Phys. Rev. E*, 72(4):046701, 2005.

[62] J. Towns, T. Cockerill, M. Dahan, I. Foster, K. Gaither, A. Grimshaw, V. Hazlewood, S. Lathrop, D. Lifka, G. D. Peterson, R. Roskies, J. R. Scott, and N. Wilkins-Diehr. XSEDE: Accelerating scientific discovery. *Comput. Sci. Eng.*, 16(5):62–74, 2014.

[63] J. E. McClure, H. Wang, J. F. Prins, C. T. Miller, and W. Feng. Petascale application of a coupled CPU-GPU algorithm simulation and analysis of multiphase flow solutions in porous medium systems. In 28th IEEE International Parallel & Distributed Processing Symposium (Phenix, Arizona), 2014.

[64] J. E. McClure, M. A. Berrill, W. G. Gray, and C. T. Miller. Influence of phase connectivity on the relationship among capillary pressure, fluid saturation, and interfacial area in two-fluid-phase porous medium systems. *Phys. Rev. E*, 94:033102, 2016.

[65] A. Fakhari, T. Mitchell, C. Leonardi, and D. Bolster. Improved locality of the phase-field lattice Boltzmann model for immiscible fluids at high density ratios. *Phys. Rev. E*, 96(053301), 2017.

[66] Y. Inoue, Y. Chen, and H. Ohashi. A mesoscopic simulation model for immiscible multiphase fluids. *J. Comput. Phys.*, 201(1):191–203, 2004.

[67] Y. Inoue, S. Takagi, and Y. Matsumoto. A mesoscopic simulation study of distributions of droplets in a bifurcating channel. *Comput. Fluids*, 35(8-9):971–977, 2006.

[68] G. Gompper, T. Ihle, D. M. Kroll, and R. G. Winkler. Multiparticle collision dynamics: a particle-based mesoscale simulation approach to the hydrodynamics of complex fluids. In Christian Holm and Kurt Kremer, editors, *Advanced computer simulation approaches for soft matter sciences III*, pages 1–87. Springer Berlin Heidelberg, Berlin, Heidelberg, 2009.

[69] R. Kapral. Multiparticle collision dynamics: simulation of complex systems on mesoscales. *Adv. Chem. Phys.*, 140:89, 2008.

[70] T. Hiller, J. Ardevol-Murison, A. Muggeridge, M. Schröter, and M. Brinkmann. The Impact of Wetting-Heterogeneity Distribution on Capillary Pressure and Macroscopic Measures of Wettability. *SPE J.*, pages SPE–194191–PA, 2018.

[71] A. Lamura and G. Gompper. Numerical study of the flow around a cylinder using multi-particle collision dynamics. *Eur. Phys. J. E*, 9(1):477–485, 2002.

[72] J. W. Cahn and J. E. Hilliard. Free energy of a nonuniform system. I. Interfacial free energy. *J. Chem. Phys.*, 28:258–267, 1958.

[73] H. G. Lee, J. S. Lowengrub, and J. Goodman. Modeling pinchoff and reconnection in a Hele-Shaw cell. I. The models and their calibration. *Phys. Fluids*, 14(2):492–513, 2002.

[74] J. Lowengrub and L. Truskinovsky. Quasi-incompressible Cahn-Hilliard fluids and topological transitions. *P. Roy. Soc. A-Math. Phy.*, 454(1978):2617–2654, 1998.

[75] J. W. Cahn. Critical point wetting. *J. Chem. Phys.*, 66(8):3667–3672, 1977.

[76] J. A. Warren, T. Pusztai, L. Környei, and L. Gránásy. Phase field approach to heterogeneous crystal nucleation in alloys. *Phys. Rev. B*, 79(1):014204, 2009.

[77] H. C. Yu, H. Y. Chen, and K. Thornton. Extended smoothed boundary method for solving partial differential equations with general boundary conditions on complex boundaries. *Modell. Simul. Mater. Sci. Eng.*, 20(7):075008, 2012.

[78] S. Osher and J. A. Sethian. Fronts propagating with curvature-dependent speed: Algorithms based on Hamilton-Jacobi formulations. *J. Contam. Hydrol.*, 79(1):12–49, 1988.

[79] J. U. Brackbill, D. B. Kothe, and C. Zemach. A continuum method for modeling surface tension. *J. Comput. Phys.*, 100(2):335–354, 1992.

[80] M. Graveleau, C. Soulaine, and H. Tchelepi. Pore scale simulation of mass transfer across immiscible interfaces. *Transp. Porous Med.*, 120(2):287–308, 2017.

[81] H. Rusche. *Computational fluid dynamics of dispersed two-phase flows at high phase fraction*. PhD thesis, Imperial College London, 2002.

[82] S. V. Patankar. *Numerical Heat and Mass Transfer*. Hemisphere Publ. Corp., Washington, 1980.

[83] R. Scardovelli and S. Zaleski. Direct numerical simulation of free-surface and interfacial flow. *Annu. Rev. Fluid Mech.*, 31:567–603, 1999.

[84] M. M. Francois, S. J. Cummins, E. D. Dendy, D. B. Kothe, J. M. Sicilan, and M. W. Williams. A balanced-force algorithm for continuous and sharp interfacial surface tension models within a volume tracking framework. *J. Comput. Phys.*, 213(1):141–173, 2006.

[85] A. Raeini, M. J. Blunt, and B. Bijeljic. Modelling two-phase flow in porous media at the pore-scale using the volume-of-fluid method. *J. Comput. Phys.*, 231(17):5653–5668, 2012.

[86] B. Issa, R.and Ahmadi-Befrui, K. Beshay, and A. Gosman. Solution of the implicitly discretised reacting flow equations by operator-splitting. *J. Comput. Phys.*, 93(2):388–410, 1985.

[87] B. van Leer. Towards the ultimate conservative difference scheme. II. Monotonicity and conservation combined in a second-order scheme. *J. Comput. Phys.*, 14(4):361–370, 1974.

[88] J. Boussinesq. Mémoire sur l'influence des frottements dans les mouvements réguliers des fluids. *J. Math. Pures Appl.*, 13:377–424, 1868.

[89] T. H. Nguyen. Hausdorff box-counting fractal dimension with multi-resolution calculation.

[90] D. Wilkinson and J. Willemsen. Invasion percolation: a new form of percolation theory. *J. Phys. A*, 16:3365–3376, 1983.

[91] M. Cieplak and M. O. Robbins. Dynamical transition in quasistatic fluid invasion in porous media. *Phys. Rev. Lett.*, 60:2042–2045, 1988.

[92] L. Furuberg, K. J. Måløy, and J. Feder. Intermittent behavior in slow drainage. *Phys. Rev. E*, 53(1), 1996.

[93] R. Lenormand, E. Touboul, and C. Zarcone. Numerical models and experiments on immiscible displacements in porous media. *J. Fluid Mech.*, 189:165–187, 1988.

[94] R. P. Mayer and R. A. Stowe. Mercury porosimetry—breakthrough pressure for penetration between packed spheres. *J. Colloid Sci.*, 20(8):893–911, 1965.

[95] H. M. Princen. Capillary phenomena in assemblies of parallel cylinders: I. Capillary rise between two cylinders. *J. Colloid Interface Sci.*, 30(1):69–75, 1969.

[96] C. Jamin, S. Pion, and M. Teillaud. 3D triangulations. In *CGAL User and Reference Manual*. CGAL Editorial Board, 4.12.1 edition, 2018.

[97] R. Chandler, J. Koplik, K. Lerman, and J. F. Willemsen. Capillary displacement and percolation in porous media. *J. Fluid Mech.*, 119:249–267, 6 1982.

SUPPLEMENTARY INFORMATION

- Supplementary Note 1: Displacement Patterns for Priority Cases

- Supplementary Note 2: Image Analysis

- Supplementary Note 3: Lattice/Particle-based Methods

- Supplementary Note 4: Continuum Methods

- Supplementary Note 5: Pore-network Models

SUPPLEMENTARY NOTE 1: DISPLACEMENT PATTERNS FOR PRIORITY CASES

This benchmark study is based on the experiments of Zhao *et al.* [2], who studied fluid-fluid displacement in a quasi-2D microfluidic flow cell over a wide range of wettabilities and capillary numbers. A total of 14 teams (see Table 1 of the manuscript) contributed modelling results to the benchmark study. Together they applied many different pore-scale modelling methods. In general, the modelling methods can be categorized into three major classes: lattice/particle-based models (Supp. Note 3), continuum models (Supp. Note 4), and pore-network models (Supp. Note 5). Lattice/particle-based models include lattice Boltzmann (LB) methods and stochastic rotation dynamics (SR) models. Continuum models include volume-of-fluid (VF) methods, level-set (LS) methods, and phase-field (PF) models. Pore-network (PN) models include quasi-static and dynamic variants. To allow for qualitative and quantitative comparisons between methods without imposing an excessive computational burden on participants, we identified four "priority cases" that best represent the diversity of patterns and physical mechanisms that emerge from fluid-fluid displacement under different Ca and wettability conditions. These priority cases include strong drainage at high Ca (SD-HC), weak imbibition at low Ca (WI-LC), strong imbibition at intermediate Ca (SI-IC), and strong imbibition at low Ca (SI-LC). We use the simulated displacement patterns at the end of the simulation, when the invading fluid reaches the outer boundary of the computational domain, as our basis for qualitative and quantitative comparison (Fig. S1 – S4).

FIG. S1: Simulated displacement patterns for strong drainage at high Ca (SD-HC). The corresponding experimental displacement pattern is presented in the top row. See Fig. 3A of the manuscript for corresponding quantitative performance results.
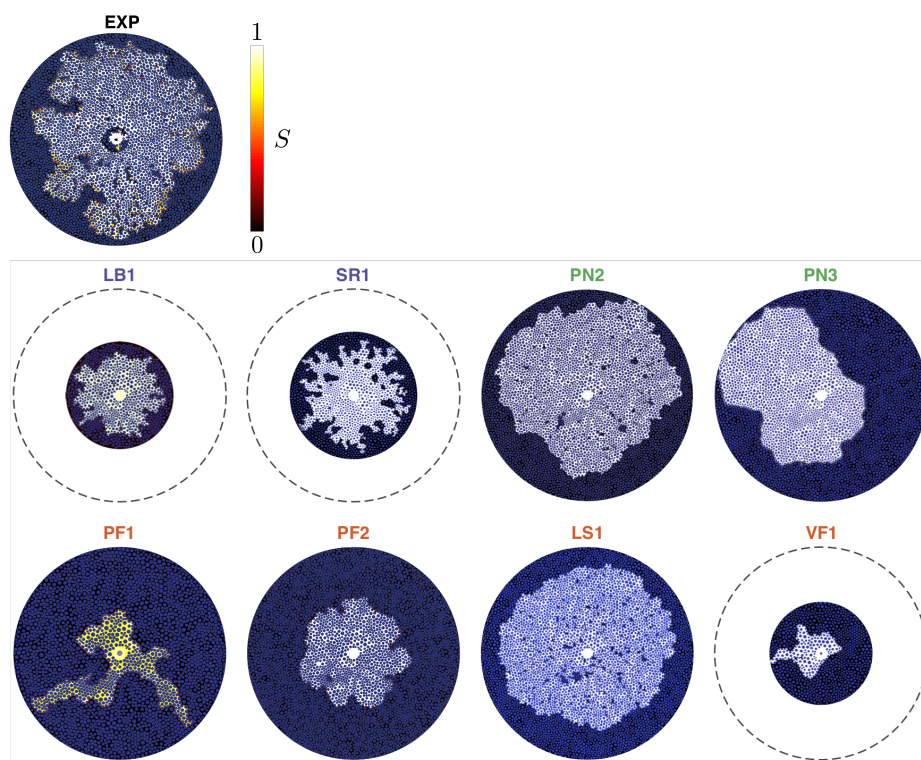
FIG. S2: Simulated displacement patterns for weak imbibition at low Ca (WI-LC). The corresponding experimental displacement pattern is presented in the top row. See Fig. 3B of the manuscript for corresponding quantitative performance results.

FIG. S3: Simulated displacement patterns for strong imbibition at intermediate Ca (SI-IC). The corresponding experimental displacement pattern is presented in the top row. See Fig. 3C of the manuscript for corresponding quantitative performance results.
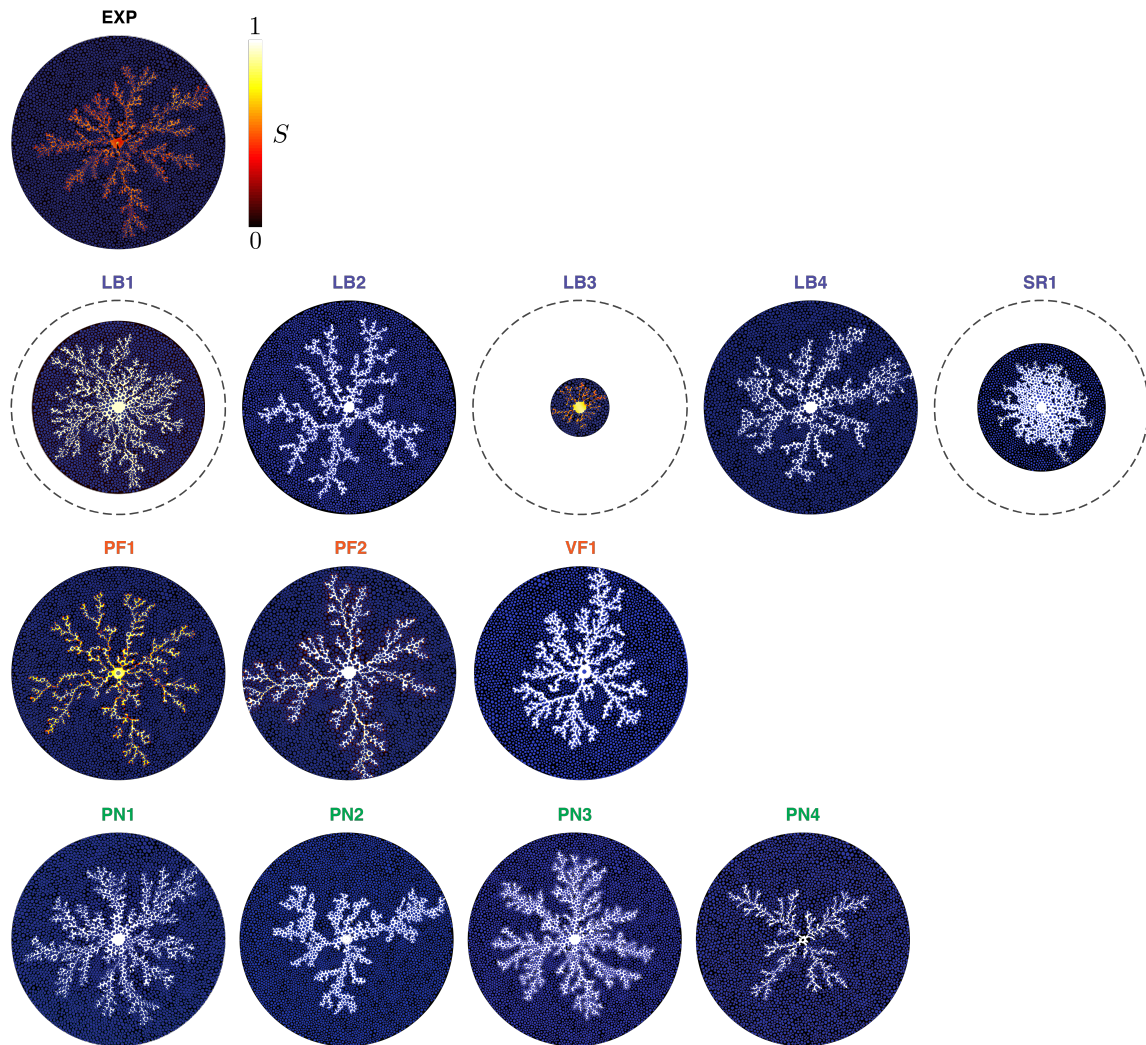
FIG. S4: Simulated displacement patterns for strong imbibition at low Ca (SI-LC). The corresponding experimental displacement pattern is presented in the top row. See Fig. 3D of the manuscript for corresponding quantitative performance results.
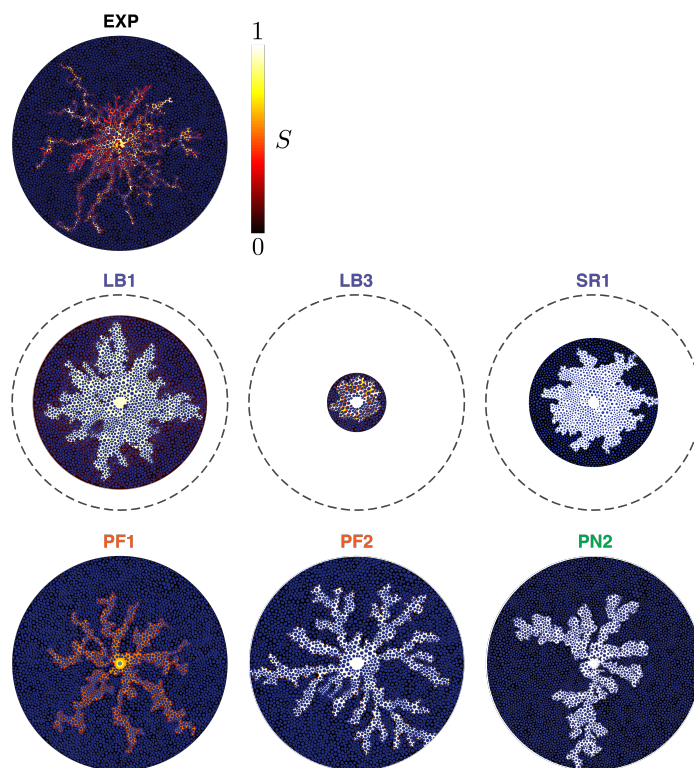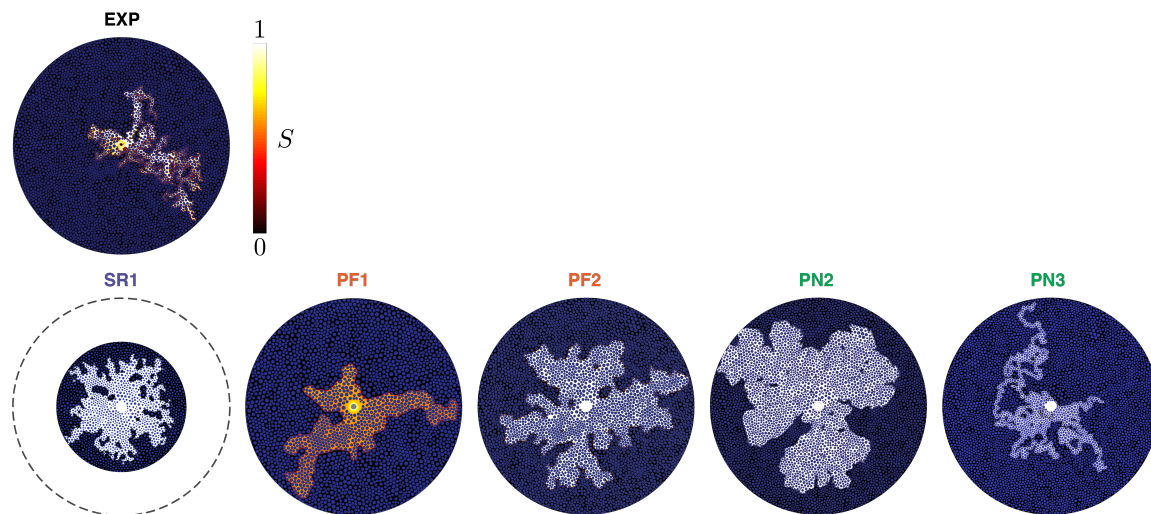
SUPPLEMENTARY NOTE 2: IMAGE ANALYSIS

We extract four performance measures from the modelling outputs for quantitative comparison.

1. Fractal dimension D_f, as calculated via the box-counting method. This is a classical measure of the degree to which a pattern fills space in 2D [40].

2. Average dimensionless finger width W_f, as measured at half the radius of the computational domain and scaled by the median post diameter (Fig. S5 c-d). Note that this measure is very sensitive to domain size for compact displacements, and that not all groups used the same domain size.

3. The gap-averaged saturation S of the invading fluid, as represented by its median value as well as the first and third quartiles (Fig. S5 a-b).

4. Displacement efficiency E_d, which is the fraction of the defending fluid that has been displaced from the domain. The total volume of the displaced defending fluid is given by the product of the gap-averaged saturation S of the invading fluid and the gap thickness, summed over the entire domain.
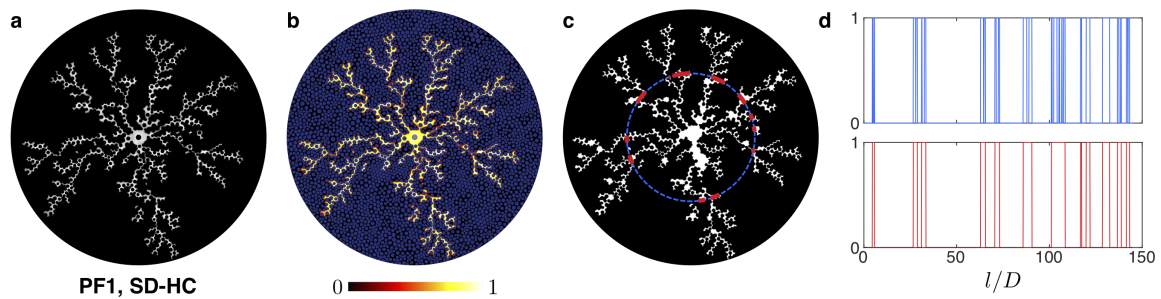

FIG. S5: Sample image analysis procedure. (a) We received simulation results in the form of high-resolution images of the displacement pattern at the end of the simulation, which is when the invading fluid reaches the edge of the simulation domain. The images are 8-bit grayscale TIFF files, with the intensity of each pixel corresponding to the gap-averaged saturation of the invading fluid. (b) We overlay the post structure onto the displacement pattern, here also displaying the gap-averaged saturation of the invading fluid via a colormap. (c) We create a binary image of invaded (white) and un-invaded (black) regions by applying a global saturation threshold. Posts that are completely surrounded by the invading fluid are treated as part of the invaded region. Using this binary image, we measure the fractal dimension D_f via the box-counting method. We measure the finger widths W_f at a radial distance that is halfway from the injection port to the outer boundary of the simulation domain (dashed blue circle). The fingers are defined as continuous stretches (red solid) of the invading fluid along the circle. (d) Top: Pixel intensity of the binary image along the circle where finger widths are measured, where l/D is the dimensionless distance along the circle with D the median post diameter. Bottom: We merge immediately adjacent fingers (i.e., those separated by a single post) to obtain a more representative measurement of finger width.

SUPPLEMENTARY NOTE 3: LATTICE/PARTICLE-BASED METHODS

Lattice Boltzmann Model 1 (LB1)

Authors: Yu Chen and Albert J. Valocchi
Email: yu_chen@lanl.gov; valocchi@illinois.edu

Introduction

The lattice Boltzmann (LB) method [6] is particularly suitable for the numerical simulation of flow of complex fluid in complex geometries. The LB color-fluid multiphase model [58] ensures a relatively sharp interface and completely immiscible fluids, and the method can be relatively easily implemented on manycore processors such as Graphical Processing Units (GPUs) to significantly increase the computing capability. Therefore, the LB color-fluid multiphase model has been widely adopted for modelling multiphase flow in porous media.

Our in-house LBM code is based on a variant of the multiple relaxation time (MRT) [59] color-fluid multiphase lattice Boltzmann model [12, 60]. The 3D code is optimized for massively parallel computing and can efficiently utilize many-core processors. Thanks to the computing capability of the code, we are able to perform 3D direct numerical simulations on the micromodel benchmark so that events like corner flow can be simulated. Benchmarking against experiments can be used to evaluate our production code, which is designed for multiphase flow simulation in 3D rocks.

Model Description: color-fluid lattice Boltzmann multiphase model

In the color-fluid model, we label different fluids with a color index, *e.g.*, fluid r (red) and fluid b (blue), which are represented by their own particle distribution function (PDF), f_i^{r} and f_i^{b}, respectively. Here i represents the ith lattice direction of the D3Q19 lattice model. The lattice Boltzmann equations for both fluids are

$$f_i^{\mathrm{s}}(\mathbf{x} + \mathbf{e}_i \delta t, t + \delta t) = f_i^{\mathrm{s}}(\mathbf{x}, t) + \Omega_i^{\mathrm{s}}(\mathbf{x}, t),\ \mathrm{s} = \mathrm{r, b},\ i = 0, ..., 18, \tag{1}$$

where superscript 's' indicates either fluid r or fluid b, $\mathbf{e}_i$ is the lattice velocity, and $\Omega_i^{\mathrm{s}}(\mathbf{x}, t)$ is the collision operator, which is comprised of three parts:

$$\Omega_i^{\mathrm{s}} = \Omega_i^{\mathrm{s}(3)}\{\Omega_i^{\mathrm{s}(1)} + \Omega_i^{\mathrm{s}(2)}\}, \tag{2}$$

where $\Omega_i^{\mathrm{s}(1)}$ is the regular LB MRT collision operator, $\Omega_i^{\mathrm{s}(2)}$ is the perturbation operator responsible for the generation of surface tension, and $\Omega_i^{\mathrm{s}(3)}$ represents the 'recoloring', which mimics the phase separation mechanism. For fluids with identical density, it is not necessary to calculate the operators $\Omega_i^{\mathrm{s}(1)}$ and $\Omega_i^{\mathrm{s}(2)}$ separately for each component. Then, Eq. (2) becomes,

$$\Omega_i^{\mathrm{s}} = \Omega_i^{\mathrm{s}(3)}\{\Omega_i^{(1)} + \Omega_i^{(2)}\}, \tag{3}$$

where $\Omega_i^{(1)}$ and $\Omega_i^{(2)}$ are the MRT collision operator and the perturbation operator for the bulk fluid mixture, respectively. Followed the work of Tölke *et al.* [60], the perturbation operator is integrated in the MRT framework by adding additional terms to the stress-related equilibrium moments. After the collision step for the bulk fluid mixture in the MRT framework, we obtain the post-collision PDFs of the fluid mixture. The recoloring operator $\Omega_i^{\mathrm{s}(3)}$ redistributes the mass distributions of fluid r and fluid b in a way so that the inner product of the color gradient and momentum of fluid r is maximized [60]. The static contact angle θ is modeled by assigning a constant order parameter value on the solid boundary nodes [61]. More details of the numerical model and implementation of the code on many-core processors can be found in [12].

Simulation Setup and Procedure

The height of the circular posts $b = 100\ \mu$m is comparable to the median pore-throat size $d = 300\ \mu$m. Therefore, either 3D simulation or 2D simulation with sub-models to account for the finite depth of the micromodel are required. Moreover, the experimental study clearly shows the importance of corner flow in the strong imbibition case. Therefore, we performed 3D simulations to avoid the approximations inherent to 2D simulations.

The details of the simulation domain and boundary conditions can be found in Fig. S6. Only the half depth of the micromodel is simulated to reduce the overall computation cost while a symmetry boundary condition is applied on the mid-plane of the cell. Our small domain tests show that there is negligible difference between the half depth and full depth simulation. We used a similar simulation set up in other studies applying LBM to micromodel experiments [12].
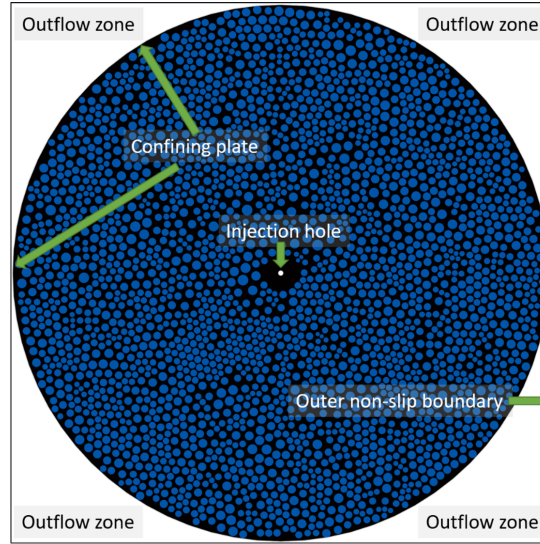
FIG. S6: Simulation domain and boundary conditions: a confining round plate covers the top of the micromodel; an injection hole is located on the center of the confining plate where constant velocity boundary condition is applied to inject the fluid; at the top of the micromodel, the rest of the areas excluding the confining plate are outflow zones, where constant pressure boundary condition is applied; at the bottom of the micromodel, symmetry boundary condition is applied; the bounce-back non-slip boundary condition is applied to all solid surfaces.
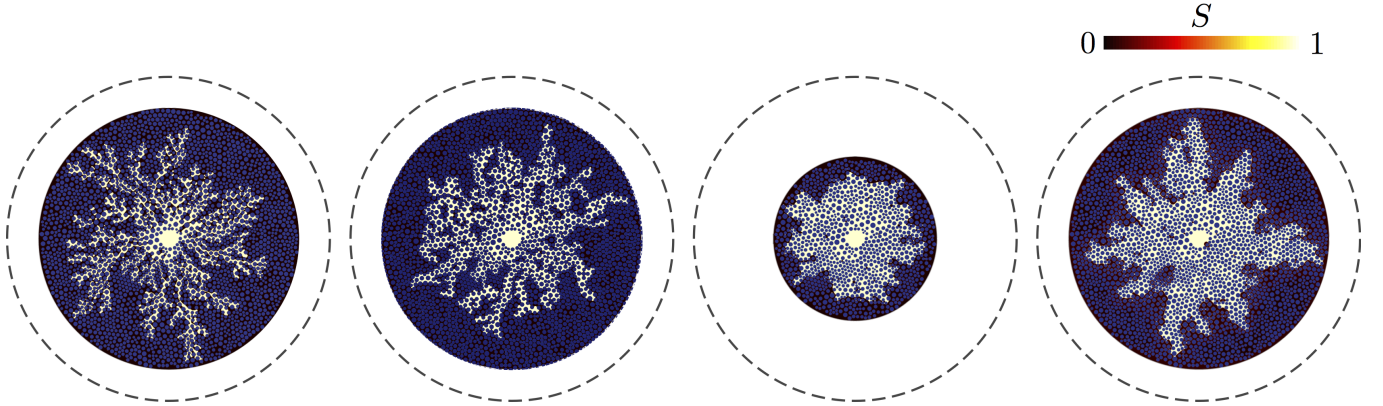

FIG. S7: Simulated displacement patterns for different wettability conditions and capillary number (left to right: Strong drainage at high Ca for $\mathcal{M} = 100$, Strong drainage at low Ca for $\mathcal{M} = 5$, weak imbibition at low Ca for $\mathcal{M} = 5$, strong imbibition at intermediate Ca for $\mathcal{M} = 40$.

Considering the computation cost and numerical accuracy, we chose a grid resolution of $14.3~\mu$m and performed the simulations on a cropped domain which covers $80\,\%$ of the diameter of the micromodel used in the experiment. The final grid for the half-depth computational domain is $5722 \times 5 \times 5722$. For WI-LC, the domain is further cropped to $50\,\%$ of the diameter of the micromodel to reduce the computational cost since WI-LC is relatively insensitive to domain size.

The capillary number is defined by $\mathrm{Ca} = \mu_{\mathrm{oil}} v_{\mathrm{inj}}/\gamma$, where v_{inj} is the characteristic injection velocity and is fixed during the simulation. Therefore, one would prefer a small ratio of μ_{oil} over γ to achieve a large injection rate in the simulation. However, in the commonly used LB models, the ratio of μ_{min} (minimum viscosity of the two fluids) over γ is constrained and typically larger than 0.1. As a result, it is very challenging to simulate the low Ca cases with high viscosity ratio $\mathcal{M}$. For instance, more than a billion iterations are required to simulate the low Ca cases at viscosity ratio $\mathcal{M} = 340$. Also, at very high viscosity ratio ($\mathcal{M} > 100$), spurious currents cause significant anisotropy of the fluid interface due to the small depth of the micromodel (the anisotropy is less severe in real 3D rock geometries). In summary, compared to the viscosity ratio of about 340 in the experiments, much smaller viscosity ratios are used in the simulations, particularly for the low Ca cases. In these low-Ca cases, as the capillary force is dominant, the viscous effects could be less important and the use of smaller viscosity ratio might be justified. The simulations were performed on the TACC Stampede 2 supercomputer provided by XSEDE [62], where the LBM

simulations benefitted from the high memory bandwidth of the Intel Xeon Phi (KNL) processor. A typical simulation took 14 KNL processors 16 to 58 hours to complete, depending on the injection rate. Fig. S7 shows the simulated displacement patterns.

Lattice Boltzmann Model 2 (LB2)

Authors: Jianlin Zhao and Qinjun Kang
Email: qkang@lanl.gov

Introduction

The color-gradient lattice Boltzmann (LB) model is adopted in this simulation. In this model, two density distribution functions are used to represent the two fluids. In addition to the regular propagation and collision steps, a perturbation operator is added to generate the interfacial tension, and a recoloring operator is added to produce the phase segregation and maintain the phase interface. Then the fluid-fluid interfaces can automatically form. To reduce the computational cost, 2D simulations of the displacements under high capillary numbers (with injection rate of 0.2 mL/min) are conducted.

Model Description

In the color-gradient LB model, there are two immiscible fluids (red and blue) represented by the distribution functions f_i^R and f_i^B, respectively. The total distribution function is defined as: $f_i = f_i^R + f_i^B$. For each fluid, the evolution equation is:

$$f_i^k(\mathbf{x} + \mathbf{e}_i \delta_t, t + \delta_t) = f_i^k(\mathbf{x}, t) + \Omega_i^k(f_i^k(\mathbf{x}, t)), \tag{4}$$

where $k = R$ or B represents the red or blue fluid; $\mathbf{x}$ is the spatial location of the particles; $\mathbf{e}_i$ is the discrete velocity in the i direction; t is time; δ_t is the time increment; Ω_i^k is the collision operator and consists of three parts: $\Omega_i^k = (\Omega_i^k)^{(3)}[(\Omega_i^k)^{(1)} + (\Omega_i^k)^{(2)}]$.

$(\Omega_i^k)^{(1)}$ is the single phase collision operator. The MRT collision operator is adopted here:

$$(\Omega_i^k)^{(1)} = (\mathbf{M}^{-1}\mathbf{S}\mathbf{M})_{ij}(f_j^k - f_j^{k,(eq)}) + \Phi_i, \tag{5}$$

where $\mathbf{M}$ is the transformation matrix which is used to map the vector $\mathbf{f}$ in discrete velocity space to the vector $\mathbf{m}$ in moment space; $\mathbf{S}$ is the diagonal collision matrix; Φ_i is the external force term.

$(\Omega_i^k)^{(2)}$ is the perturbation operator which generates an interfacial tension:

$$(\Omega_i^k)^{(2)} = \frac{A^k}{2} \left|\nabla \rho^N\right| \left(w_i \frac{(\mathbf{e}_i \cdot \nabla \rho^N)^2}{|\nabla \rho^N|^2} - B_i \right), \tag{6}$$

where ρ^N is the phase field function; A^k is a function related to the interfacial tension.

$(\Omega_i^k)^{(3)}$ is the recoloring operator used to produce the phase segregation and maintain the phase interface:

$$
\begin{aligned}
(\Omega_i^R)^{(3)}(f_i') &= \frac{\rho^R}{\rho} f_i' + \beta w_i \frac{\rho^R \rho^B}{\rho^2} \cos(\varphi_i) f_i^{eq}|_{\mathbf{u}=0} \\
(\Omega_i^B)^{(3)}(f_i') &= \frac{\rho^B}{\rho} f_i' + \beta w_i \frac{\rho^R \rho^B}{\rho^2} \cos(\varphi_i) f_i^{eq}|_{\mathbf{u}=0}
\end{aligned}
\tag{7}
$$

where f_i' is the post-perturbation total distribution function; φ_i is the angle between the color gradient $\nabla \rho^N$ and the lattice direction $\mathbf{e}_i$; and β is a parameter related to the interface thickness.

The no-slip halfway bounce-back boundary condition is applied at the solid walls. To generate a certain contact angle, the solid node is assumed to be a mixture of two fluids and has a certain value of the phase field ρ_s^N. If the contact angle of the red fluid is θ^R, ρ_s^N should be set as $\cos \theta^R$. More details about the model can be found in the references [14, 15].

Numerical setup

The size of the simulation domain is 4960×4960 and the resolution is 20.18 μm/lattice. Constant pressure boundary conditions are adopted on the four sides and constant velocity boundary conditions are adopted in the middle of the domain. All the simulations are carried out using the high performance computer cluster Grizzly of Los Alamos National Laboratory. 80×80 CPU cores are adopted with the simulation domain in each core being 62×62 lattices.

The simulation results under different wettability conditions are shown in Fig. S8. Because of the physical difference between 2D and 3D fluid flow, the simulation results show some difference from the experimental results, especially for the strong imbibition case (the rightmost subfigure). In the experiments, the water phase mainly invades the porous media along the solid surfaces in strong imbibition. However, this phenomenon cannot be properly accounted for in our 2D simulation, which results in the significant difference.
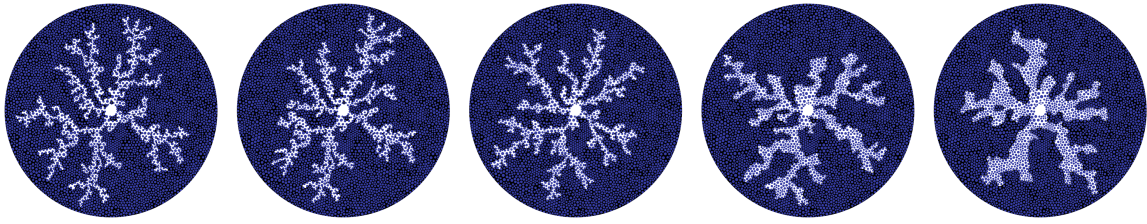
FIG. S8: Simulated fluid-fluid displacement patterns for Ca $= 2.9$ under different wettability conditions (left to right: $\theta = 150°$, $\theta = 120°$, $\theta = 90°$, $\theta = 60°$, $\theta = 7°$).

Lattice Boltzmann Model 3 (LB3)

Authors: Kelsey Bruning, James E. McClure, Cass T. Miller
Email: casey_miller@unc.edu

Introduction

The lattice Boltzmann simulator relies on the color model with a multiple-relaxation time D3Q19 collision operator for the momentum transport and a D3Q7 scheme for the mass transport. Information on the formulation, including validation of the approach used to set the contact angle can be found in the literature [16, 17]. The method is implemented in parallel using MPI and CUDA with in-situ analysis tools to track various measures of flow [63, 64]. A digitized 3D version of the microfluidic flow cell was created based upon the custom code developed to assign the position of the posts, top and bottom plates, and the flow inlet.

Model Description

The original experimental images have a resolution of 2048×2048 pixel squared with a pixel width of 54 μm. The median pore-throat size, d_{exp}, is 300 μm and the physical depth of the system, b_{exp}, is 100 μm. The diameter of the sample is 10 cm. At the original resolution, the depth of the system is less than two pixels, which is insufficient to resolve the interface profile. The simulations are performed to resolve the physical depth of the sample to 32 voxels where $d_{\text{sim}} = 32\delta x$. Sufficient resolution of the vertical direction is critical to be able to resolve pendular rings that fill the corners where each post meets the top and bottom plates. The total size of the simulation domain was $3072 \times 3072 \times 32$ with a voxel width of $\delta x = 13$ μm. This corresponds to a diameter of 4 cm. The aspect ratio of the experimental system will tend to privilege the role of capillary film dynamics on the top and bottom plates due to relative thickness of these films compared to the system depth.

The total rate of flux was specified using a volumetric flux boundary condition to match the reported flow rates, determined based upon the experimental capillary number. The capillary number was defined based upon the dynamic viscosity of the silicone oil phase, μ_{oil}; the flow rate of the invading fluid, Q; the median pore throat length, d; the depth of the media, b; and the interfacial tension between the water phase and silicone oil phase, γ. Each quantity can be evaluated in the relevant experimental units as well as the units for the simulation. To match the experimental capillary number and experimental flow rate in the simulation, simulated values are chosen to satisfy

$$\text{Ca}_{\text{sim}} = \text{Ca}_{\text{exp}} \quad \rightarrow \quad \frac{\mu_{\text{oil,sim}}Q_{\text{sim}}}{b_{\text{sim}}d_{\text{sim}}\gamma_{\text{sim}}} = \frac{\mu_{\text{oil,exp}}Q_{\text{exp}}}{b_{\text{exp}}d_{\text{exp}}\gamma_{\text{exp}}} \quad \rightarrow \quad Q_{\text{sim}} = \left(\frac{b_{\text{sim}}d_{\text{sim}}\gamma_{\text{sim}}}{\mu_{\text{oil,sim}}}\right)\text{Ca}_{\text{exp}}. \tag{8}$$

This choice establishes the basis for unit conversions between the simulated and experimental system and establishes the relationship between the lattice time step and physical time. The flux specified in the simulation provides the change in volume per unit time, where the unit of length is the lattice length and the unit of time is the lattice time. The relationship of the lattice length δx to physical units is given by h. The relationship between the physical timestep, dt, and the lattice time, δt, is chosen so that the experimental and simulated flux will match,

$$dt = \frac{Q_{\text{sim}}}{Q_{\text{exp}}} \frac{h^3}{\delta x^3} \delta t. \tag{9}$$

An attempt was made to match the mobility ratio, $\mathcal{M} = 343$. This represents a challenge for this particular LBM implementation and it was only possible to achieve $\mathcal{M} = 100$. Furthermore, the experimental and simulated density ratios do not match. The parameter values for the simulation are shown in comparison to experimental values in Table II. The simulated displacement patterns are shown in Fig. S9.

TABLE II: Parameter values for the experiment and simulation, where m, l and t are the simulated units of mass, length and time.

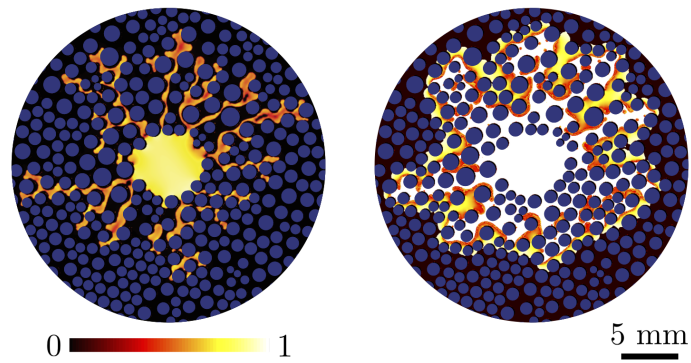| Parameter	Experiment	Simulation
R_{inlet}	1018 μm	326 l
μ_{water}	0.99 mPa·s	1/300 m/lt
μ_{oil}	340 mPa·s	1/3 m/lt
b	300 μm	300/32 l
d	100 μm	32 l
γ	13 mN/m	0.0058 m/t^2

FIG. S9: Simulated displacement patterns for strong drainage at high capillary number (left) and for strong imbibition at intermediate capillary number (right).

Lattice Boltzmann Model 4 (LB4)

Authors: Abbas Fakhari and Diogo Bolster
Email: afakhari@nd.edu

Introduction

The phase-field-based lattice-Boltzmann method (LBM) consists of an interface-tracking lattice Boltzmann equation (LBE) based on the conservative phase-field model and a pressure-evolution LBE for recovering the hydrodynamic properties [18]. The implemented phase-field LBM has been shown to be capable of dealing with realistic density and viscosity ratios while maintaining numerical stability and accuracy [19].

Model Description

All the details of the model are described in Ref. [19]. It has been shown that the phase-field LBM provides reasonably accurate results compared with experiments in a porous micromodel at relatively low density ratios [19], which is also the case in the present study. Please note that for dealing with multiphase flow dynamics at higher density ratios, the improved phase-field method recently proposed in Ref. [65] provides more accurate results.
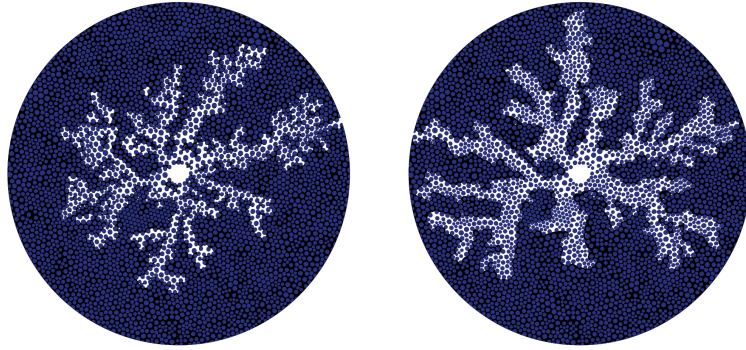

FIG. S10: Simulated fluid-fluid displacement pattern for Ca = 2.9 under two wettability conditions (left: $\theta = 150°$; right: $\theta = 60°$).

Stochastic Rotation Dynamics 1 (SR1)

Authors: Thomas Hiller and Martin Brinkmann
Email: thiller@eonerc.rwth-aachen.de

Introduction

For this benchmark study on immiscible fluid displacement, we use our custom-made 3D multi-color (multi-phase) stochastic rotation dynamics (SRDmc) algorithm [20, 66, 67]. In addition to the standard 2D SRDmc algorithm of Inoue *et al.* [66], our implementation also accounts for rigid walls with different surface wettability and angular momentum conservation.

SRD methods in general are particle based simulation techniques for modeling fluid flows, where the microscopic dynamics of the fluid particles is modeled using a sequence of streaming and collision steps. Compared to Molecular Dynamics (MD) or Dissipative Particle Dynamics (DPD) simulations, SRD requires significantly less time averaging, and allows using coarser time steps, to represent fluid motion in the continuum limit. For an extensive overview of the SRD method, we refer the reader to Refs. [68, 69].

So far, we successfully applied our Stochastic Rotation Dynamics multi-color model (SRDmc) code to study immiscible displacement in a flat microfluidic cell with cylindrical posts [21] and three-dimensional bead packs exhibiting spatial wetting heterogeneities [70].

Model Description

The algorithm used here is similar to the majority of off-lattice, particle-based, simulation methods, including the standard SRD algorithm for single phase fluids [68, 69], in providing an effective scheme to exchange linear momentum between fluid particles. During streaming, particles move deterministically between time t and $t + \Delta t$

$$\mathbf{x}_i(t + \Delta t) = \mathbf{x}_i + \mathbf{v}_i(t)\Delta t + \frac{f_{\text{ext}}}{2m_i}\Delta t^2 \tag{10}$$

with $\mathbf{x}_i$ and $\mathbf{v}_i$ being the corresponding position and velocity of particle i and f_{ext} being a constant external force acting on the particles. In order to exchange linear momentum (via collisions), the particles are sorted into cubic collision cells of side length a where the number of particles per cell fluctuates around an average value $\langle N \rangle$. The particle velocities $\mathbf{v}_i(t + \Delta t)$ after a collision are related to the pre-collisional velocities $\mathbf{v}'_i(t + \Delta t)$ through

$$\mathbf{v}_i(t + \Delta t) = \mathbf{u}(t + \Delta t) + \mathbf{\Omega}\left[\mathbf{v}'_i(t + \Delta t) - \mathbf{u}(t + \Delta t)\right] \tag{11}$$

where u is the center of mass velocity of fluid particles in the corresponding collision cell while $\mathbf{\Omega}$ denotes the collision operator. By construction, the collision operator conserves mass, linear and angular momentum, which implies that averaged local quantities such as density, stresses and flow velocity obey certain macroscopic transport equations. To ensure a constant and uniform temperature, we apply a cell level thermostat as described in [20]. The distribution of local capillary and viscous stresses in the fluids is directly obtained from averages of the momentum flux over a dense mesh of small control planes.

To simulate the flow of two immiscible fluids in the benchmark set-up, we adapted the SRDmc collision operator of Inoue *et al.* [66] that actively drives a segregation between fluid particles with different particle species (colors). In addition, to capture the impact of surface wettability on the fluids, we extended Inoue's SRDmc algorithm to account for different relative adhesion of the fluids to the surfaces of the cylindrical posts. The relative adhesion of the fluids to the surface is controlled by the color (wetting or non-wetting) of virtual ghost or wall particles inside the posts. These wall particles initially have been proposed to eliminate slip effects at the wall [71]. In every collision step, the fluid particles interact with wall particles in the same collision cell. The color and density of the wall particles (i.e. the number of particles per cell), determines the equilibrium contact angle of the fluid interface with the wall. For details of the simulation method, our implementation of surface wettability, and further benchmark tests, we refer the reader to Hiller *et al.* [20].

Numerical Setup

For the technical specifications of our implementation, please see Tab. III. Because SRD is a coarse-grained particle based method to simulate flows, we need to respect specific limitations of the simulation method. For instance, in this set-up and for the chosen simulation parameters, the viscosity contrast is controlled by the particle mass of the corresponding fluid phase. To keep the total number of fluid particles in the simulation domain fixed, we collect defending phase particles from the boundaries of the domain and insert them at the central inlet as invading phase particles. With this relocation, we change their color, mass and corresponding particle velocity. This "pump rate" stays constant over time and effectively determines the capillary number

Ca. If the viscosity ratio is too large, this protocol would result in a strong increase of the density of low-viscous invading phase particles in the inlet region. If, at the same time, the high-viscous defending fluid particles do not reach the domain boundaries at the same rate as particles are inserted in the center of the cell, this would violate the necessity for a rather constant average particle density across the whole domain.

In order to balance the need for sufficient system sizes and resolution to obtain statistically significant quantities with the computational costs of our simulation method, we limited the domain height to $5a$. Because of the small vertical dimension of the cell, the average aspect ratio of obstacles is $D/H = 3.5/5$ and therefore, the vertical fluid saturation distribution (gap-averaged saturation) is not representative. We adopt the definition of Ca described in Zhao *et al.* [2]: Ca$= \eta_{\mathrm{def}} v_{\mathrm{inv}}/\gamma$ with $v_{\mathrm{inv}} = \langle Q \rangle / L_z \langle d \rangle$, where $\langle Q \rangle$ and $\langle d \rangle = 2.33a$ are the average volume flow rate of the invading phase and the median throat diameter, respectively. The dynamic viscosity of the defending phase is denoted by η_{def} and γ is the interfacial tension between invading and defending phase.

TABLE III: Technical specifications of the SRDmc simulations

| Property	Value
Simulation domain size	$L_x \times L_y \times L_z = 300 \times 300 \times 5$ (cubic cells)
Number of cells	831744 (including 2 virtual layers on each boundary – needed for wettability implementation)
Particle density	14 particles per cell
Number of particles	4914000
Number of obstacles	1925
Porosity	0.67
Number of parallel threads	20 (OpenMP)
Memory consumption	9.5 GB
Run time per simulation	1-4 weeks depending on Ca
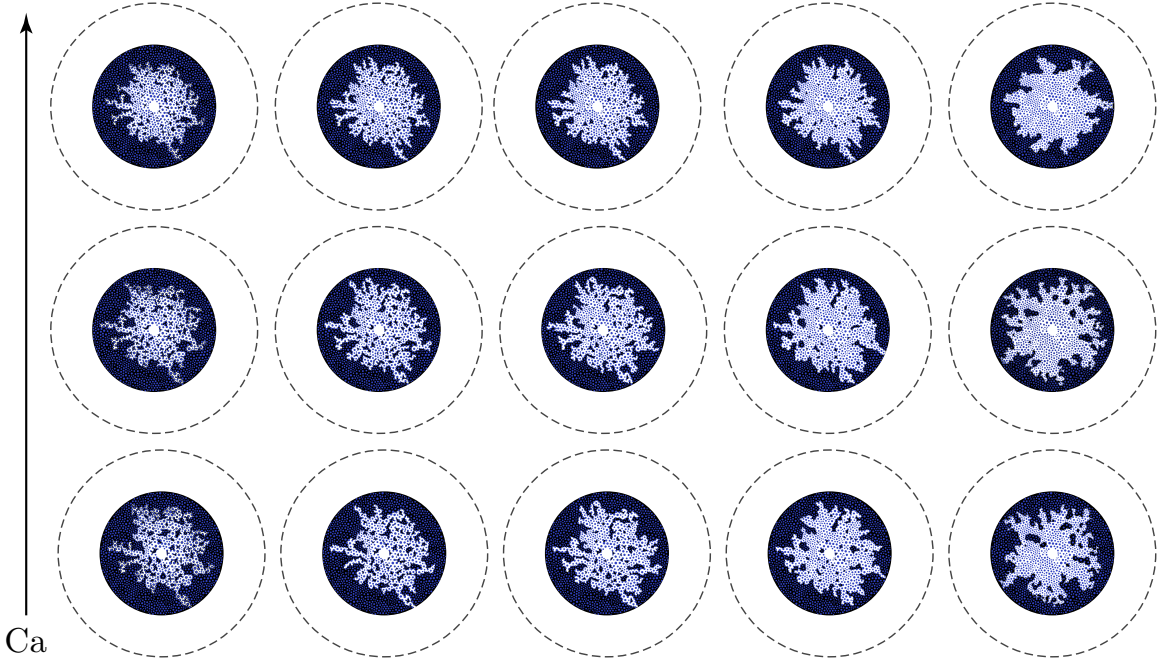
FIG. S11: Simulated displacement patterns for different wettability conditions (left to right: $\theta = 180°$, $\theta = 120°$, $\theta = 90°$, $\theta = 60°$, $\theta = 0°$) and capillary numbers. The viscosity ratio between the defending fluid and the invading fluid was set to $\mathcal{M} = 5$.

SUPPLEMENTARY NOTE 4: CONTINUUM METHODS

Phase-field Model 1 (PF1)

Authors: Luis Cueto-Felgueroso
Email: luis.cueto@upm.es

Introduction

We use a diffuse-interface model of two-phase flow to simulate the benchmark problem. The model builds on our previous work on two-phase flow in a capillary tube [23] and a Hele-Shaw cell [22], incorporating the effect of wetting conditions at the posts. This model aims at capturing the 3D viscous and capillary coupling between fluids in the cell gap via a 2D, gap-averaged Darcy formulation. In this case, the model and its outputs are different from the classical problem of approximating the 2D sharp-interface problem. Fluid volume fractions can be understood as phase fields, because they are used to represent the idea that either fluid may fully occupy the cell gap. The current model is limited by the assumption of Darcy flow in the cell gap, which may not be realistic when pore throat sizes are comparable to the cell gap width.

Model Description

Assuming constant gap width b, density-matched fluids with constant densities, and using the water saturation S_w, total pressure p and capillary pressure potential Ψ as primary variables, the model equations read [22, 23]

$$\partial_t S_\text{w} + \nabla \cdot (-\lambda_\text{w} \nabla p + \lambda_\text{w} \nabla \Psi) = 0, \tag{12}$$

$$\Psi = -c_2 F_0' + c_4 \nabla^2 S_\text{w}, \tag{13}$$

$$\nabla \cdot (-\lambda_T \nabla p + \lambda_\text{w} \nabla \Psi) = 0, \tag{14}$$

where we used the constraint $S_\text{w} + S_\text{o} \equiv 1$. The saturation-dependent phase mobilities, λ_α, and total mobility, λ_T, are defined as:

$$\lambda_\text{w} = \frac{k}{\mu_\text{w}} k_\text{rw}, \qquad \lambda_o = \frac{k}{\mu_\text{o}} k_\text{ro}, \tag{15}$$

$$\lambda_T = \lambda_\text{w} + \lambda_o = \frac{k}{\mu_\text{w}} \left(k_\text{rw} + \frac{1}{\mathcal{M}} k_\text{ro} \right), \tag{16}$$

where μ_α is the dynamic viscosity of phase α, $\mathcal{M} = \mu_\text{o}/\mu_\text{w}$ is the viscosity ratio, and the effective permeability for Darcy flow is $k = \frac{b^2}{12}$. The partial derivative of the dimensionless bulk free energy with respect to water saturation, F_0', is taken as:

$$F_0' = 16 S_\text{w} (1 - S_\text{w})^7 (1 - 5 S_\text{w}), \tag{17}$$

which is derived from a simple double-well dimensionless bulk free energy that is independent from the contact angle at the posts:

$$F_0 = 8 (1 - S_\text{w})^8 S_\text{w}^2. \tag{18}$$

The capillary pressure Ψ—equation (13)—is obtained as minus the variational derivative of a phenomenological free energy functional, $\Psi = -\delta F / \delta S_\text{w}$, where the free energy density $F(S_\text{w}, \nabla S_\text{w})$ is given by [72]:

$$F = c_2 F_0 + \frac{c_4}{2} |\nabla S_\text{w}|^2. \tag{19}$$

The parameters c_2 [N/m^2] and c_4 [N] control the effective surface tension γ and interface thickness δ, such that $c_2 \sim \gamma/\delta$ and $c_4 \sim \gamma\delta$. We used these parameters to match the experimental surface tension, $\gamma = 0.013$ N/m^2, while ensuring an interface thickness that can be resolved with affordable computational grids.

We employ relative permeability functions that reflect the preferential wetting as well as the large viscosity contrast:

$$k_{\text{rw}} = S_{\text{w}}^3 - \frac{3}{2\mathcal{M}} S_{\text{w}} (1 - S_{\text{w}})(1 + S_{\text{w}}), \tag{20}$$

$$k_{\text{ro}} = \frac{(1 - S_{\text{w}})^2 (2 + S_{\text{w}})}{2}. \tag{21}$$

The model equations (12)–(14) describe the evolution of the two-dimensional, gap-averaged fields: the vector fields are two-dimensional and the saturations, pressures and velocities should be understood as gap-averaged quantities.

Inlet and outlet boundary conditions

We impose the experimental injection rates by setting an inward volumetric water flux, V_I [m/s], along the boundary of an inlet circular injection port at the center of the domain. The radius of the injection port is $r_I = 1$ mm, and the imposed volumetric flux is

$$V_I = \frac{Q_f}{2\pi r_I b}, \tag{22}$$

where Q_f is the experimental flow rate, $Q_f = 0.002, 0.02, 0.2$ ml/min. We also impose a water saturation of 1 at the inlet boundary, $S_w = 1$. At the outer boundary of the domain, we impose a constant reference pressure, $p = 0$.

Wettability condition at the posts

We enforce the static contact angle at the posts through the simplified boundary condition:

$$\mathbf{n} \cdot \nabla S_{\text{w}} = \cos\theta |\nabla S_{\text{w}}| \tag{23}$$

Model calibration (parameters c_2 and c_4)

We calibrate parameters c_2 and c_4 by computing the steady-state solution of a water slug in a narrow channel (Figure S12). The width of the channel corresponds to a typical pore throat of 300 μm. The capillary pressure is given by $\Delta p_c = \gamma \cos\theta (2/b + 2/w)$, where $\gamma = 0.013$ N/m, $b = 100$ μm is the channel gap size, and $w = 300$ μm is the channel width. For $\theta = 45°$ we expect a capillary pressure $\Delta p_c \approx 245$ Pa. By choosing appropriate c_2 and c_4, we may in principle model the same effective surface tension with different interfacial widths, $c_2 \sim \gamma/\delta$ and $c_4 \sim \gamma\delta$. As the dynamic interface width is smaller than that obtained for a static interface, we chose values that yield a sufficiently large interface at equilibrium, so that moving interfaces can be adequately resolved. Thus, we set $c_2 = 1300$ N/m^2 and $c_4 = 3 \cdot 10^{-5}$ N. The steady-state saturation and pressure fields, as well as the profiles of saturation and pressure along the channel center line are shown in Fig. S12.
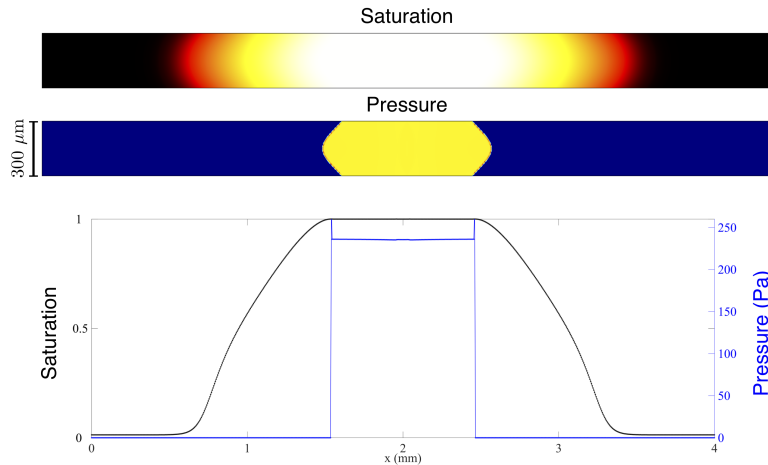

FIG. S12: Model calibration. We choose c_2 and c_4 by computing the steady-state solution of a water slug in a narrow channel, whose width corresponds to a typical pore throat size of 300 μm. For a static contact angle $\theta = 45°$ we expect a capillary pressure $\Delta p_c \approx 245$ Pa. Here we show the steady-state saturation and pressure fields, as well as the profiles of saturation and pressure along the channel center line.

TABLE IV: Summary of model parameters.

r_I	b_i	V_I	k	μ_w	M	c_2	c_4
1 mm	0.1 mm	$Q_f/(2\pi r_I b)$	$b^2/12$	10^{-3} Pa· s	339	1300 Pa	$3\cdot 10^{-5}$ N

Summary of model parameters

A summary of the model parameters is presented in Table IV. The complete model is specified by the field equations (12)–(14), together with the constitutive relations (15)–(16), (17) and (20)–(21).
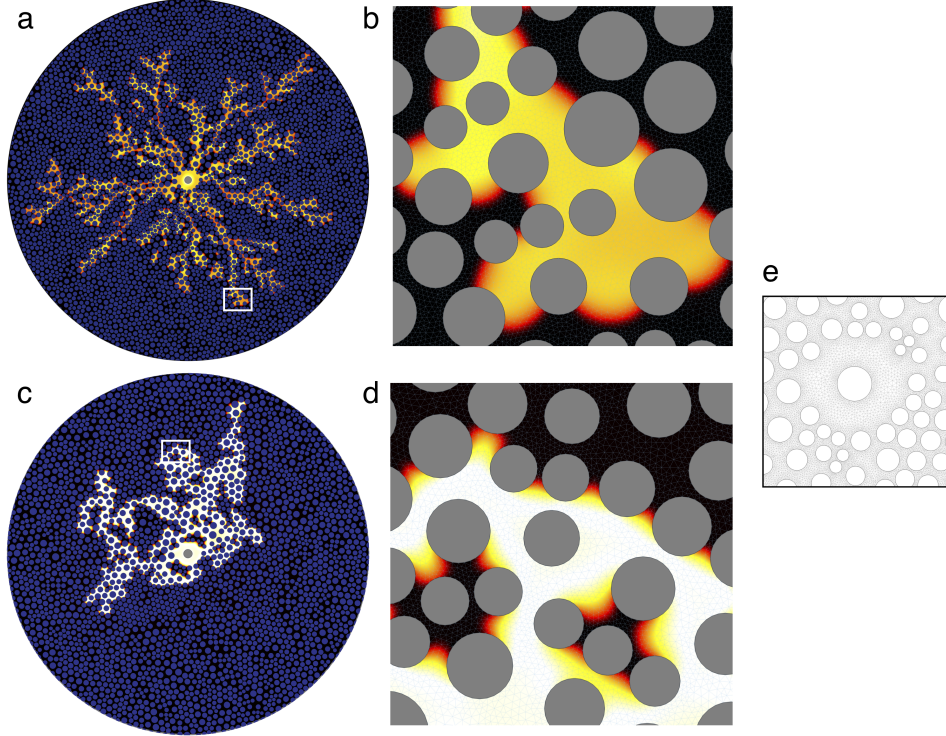

FIG. S13: Computational grids. Zoom views of the saturation field and computational grids for two sample simulations: (a, b) A sample simulation at high capillary number, which yields unsaturated fingers; (c, d) A sample simulation at low capillary number, which leads to a sharp transition between fully saturated fingers and the displaced oil. (e) Detail of the computational grid near the injection port at the center of the domain.

Implementation and grid resolution

The system of second-order PDEs (12)–(13) is discretized using standard Galerkin finite elements, with monolithic coupling between pressure and saturation. The computational grid for the full domain involves $\sim$ 1 million elements, with a typical resolution of 5-10 elements across pore throats. Fluid-fluid interfaces seem smooth with this grid resolution, although a complete refinement study has not been performed. In short, the simulations were run using the largest affordable grid that yields a large enough interfacial width. Figure S13 shows close-up views of the saturation fields and computational grids for two sample simulations: a high Ca simulation that yields unsaturated fingers (Fig. S13a–b), and a low Ca that leads to sharp transitions between fully saturated fingers and the displaced oil (Fig. S13c–d). We also show a detail of the computational grid near the injection port at the center of the domain (Fig. S13e).

Results

The simulated phase diagram is shown in Figure S14. The model seems to captures the transitions in fractal dimension and displacement efficiency across the different flow rates and wetting conditions. A remarkable feature is the ability to predict significant changes in gap-averaged saturation, which follow the experimental trends reasonably well. A notable and interesting discrepancy with experiments is the inability of the model to reproduce the patterns of compact displacement for the imbibition cases at low capillary numbers. This is probably due to the role of wetting conditions at the top and bottom plates, which is not considered here, to the choice of parameters c_2 and c_4, and to the functional form of the constitutive relationships (bulk
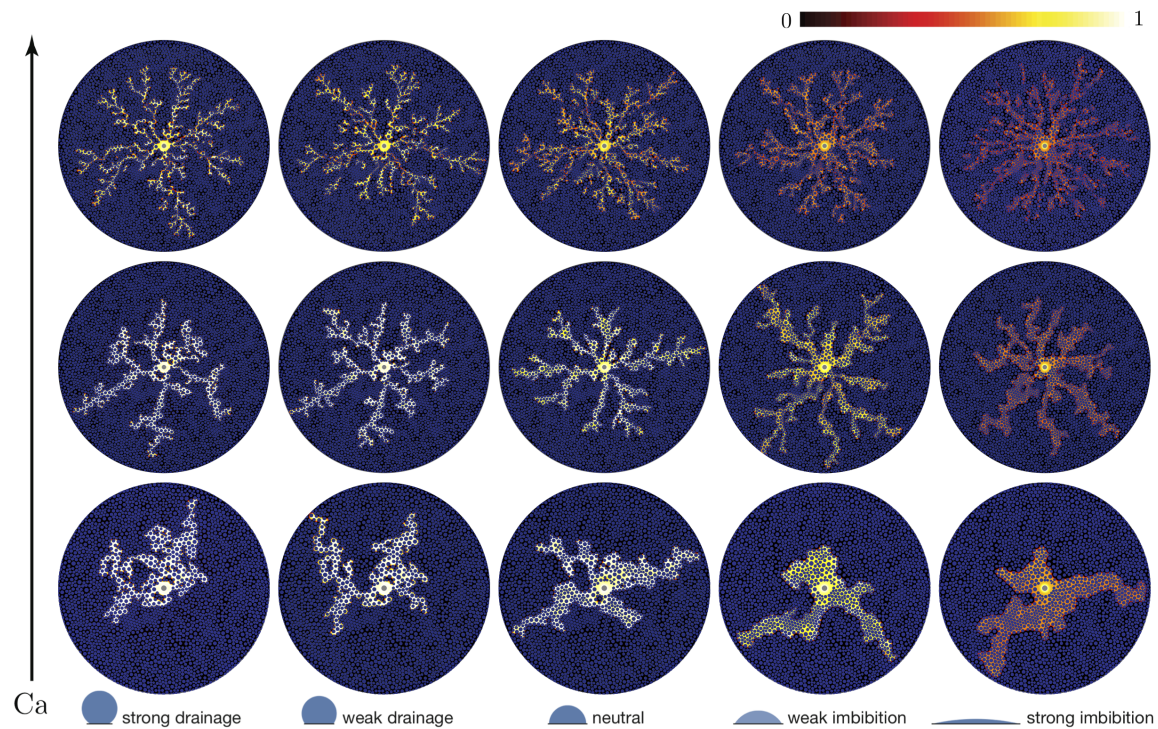
FIG. S14: Simulated displacement patterns for different wettability conditions (left to right: $\theta = 150°$, $\theta = 120°$, $\theta = 90°$, $\theta = 60°$, $\theta = 7°$) and flow rates (top to bottom: $Q_f = 0.2$ ml/min, $Q_f = 0.02$ ml/min, and $Q_f = 0.002$ ml/min).

free energy and relative permeabilities). Another obvious discrepancy is the absence of a sharp wetting transition for the strong imbibition case. While there is a clear morphological difference between experimental displacement patterns of $\theta = 60°$ and $\theta = 7°$, the model predicts qualitatively similar displacement patterns. Capturing the displacement processes observed in strong imbibition would require incorporating wetting and flow processes that are not captured in the present gap-averaged model. Among them is the assumption of Darcy flow in the gap, which probably does not represent the complex 3D flow processes that may ensue in the case of narrow throats of a width that is comparable to the cell gap.

Phase-field Model 2 (PF2)

Authors: Daniel A. Cogswell
Email: cogswell@alum.mit.edu

Introduction

A depth-averaged phase-field model was developed for simulating oil/water displacement through arbitrarily complex pore structures with a controllable contact angle at the solid pore walls. Phase-field models are advantageous because they capture the Laplace pressure jump across curved interfaces without the need to explicitly track boundaries. The model is based on the Cahn-Hilliard-Hele-Shaw system of equations, which describes depth-averaged fluid flow between two parallel plates (*i.e.* a Hele-Shaw cell). This model is an extension of a previous model for Darcy flow [24] with a variational boundary condition introduced to specify the contact angle boundary condition at pore walls, and with the choice of linear relative permeability functions.

Model Description

The evolution equations for the Cahn-Hilliard-Hele-Shaw phase-field model are [73, 74]:

$$\frac{\partial \xi}{\partial t} + \nabla \cdot (\xi \vec{v}) = \frac{1}{Pe} \nabla \cdot \left(M \vec{\nabla} \hat{\mu} \right) + q_w \tag{24a}$$

$$\nabla \cdot \vec{v} = q_t \tag{24b}$$

$$\vec{v} = -\frac{b^2}{12\eta(\xi)} \left[\vec{\nabla} p - \mu \nabla \xi \right] \tag{24c}$$

The first equation is a convective Cahn-Hilliard equation, the second is a continuity equation, and the third equation is a generalized form of Darcy's law, where $\frac{b^2}{12}$ is the depth-averaged permeability of fluid flowing between two parallel plates separated by a distance b. The order paramter ξ varies smoothly across the interface between the two fluids, taking the equilibrium values of $\xi = 0$ in the oil phase, and $\xi = 1$ in the water phase. Pressure is p, $\vec{v}$ is the Darcy velocity of the fluid, $\hat{\mu}$ is a diffusion potential, and Pe is a dimensionless Peclet number. M is mobility, taken to be $M = \frac{b^2}{12\eta_w}$. The injection/production rate of water is q_w, and $q_t = q_w + q_o$ is the total injection/production rate of both fluids. The viscosity function $\eta(\xi)$ in Eq. (24c) was chosen to the be the following mixture interpolation function:

$$\eta(\xi) = \eta_w e^{R(1-\xi)} \tag{25a}$$

$$R = \ln(\eta_o/\eta_w) \tag{25b}$$

In the phase-field approach, the diffusion potential $\hat{\mu}$ is the variational derivative of a free energy functional that includes a gradient term to capture interfacial energy:

$$F = \int H f(\xi) + \frac{1}{2}\kappa |\vec{\nabla}\xi|^2 \, dV \tag{26a}$$

$$\hat{\mu} = \frac{\delta F}{\delta \xi} = H f'(\xi) - \kappa \nabla^2 \xi \tag{26b}$$

where $f(\xi) = \xi^2(1-\xi)^2$ is a double-well free energy function and H and κ are constants. For this choice of $f(\xi)$, the oil-water interfacial energy is $\gamma = \sqrt{\frac{\kappa H}{18}}$ and the width of the diffuse interface is $W = \sqrt{\frac{8\kappa}{H}}$. The Peclet number is chosen to be $Pe = \frac{1}{\sqrt{\kappa}}$ based on asymptotic analysis [73, 74].

To simulate the effect of wetability alterations, the contact angle of the oil-water interface at the pore walls was specified with a contact angle boundary condition derived elsewhere [75, 76]:

$$\vec{n} \cdot \vec{\nabla}\xi = \sqrt{\frac{2\Delta f}{\kappa}} \cos(\theta) \tag{27}$$

where $\vec{n} = \vec{\nabla}\xi/|\vec{\nabla}\xi|$ is the normal to the surface of the pore wall and θ is the contact angle.

To apply boundary conditions at complex pore geometries, a parameter Ψ was defined such that $\Psi = 1$ in the pore space (domain of simulation), and 0 everywhere else. Images of the pore structure were used to generate Ψ, which was then incorporated into the evolution equations following the smooth boundary method [77]. The resulting equations are:

$$\frac{\partial \xi}{\partial t} = -\nabla \cdot (\Psi \xi \vec{v}) + \nabla \cdot \left(\Psi M \vec{\nabla} \hat{\mu} \right) + \Psi q_w \tag{28a}$$

$$\hat{\mu} = H f'(\xi) - \kappa \left[\nabla \cdot \left(\Psi \vec{\nabla} \xi \right) + |\nabla \Psi| \sqrt{\frac{2\Delta f}{\kappa}} \cos(\theta) \right] \tag{28b}$$

$$\nabla \cdot (\Psi \vec{v}) = \Psi q_t \tag{28c}$$

This is the set of evolution equations solved to simulate the benchmark problem. For numerical efficiency the capillary stress tensor in Eq. (24c), $-\mu\nabla\xi$, was set to zero and not included in the calculations.

The numerical treatment of Eq. (28) was very similar to that presented in Ref. [24]. The equations were discretized using finite volumes, and solved using FAS multigrid with bilinear restriction and interpolation, and semi-implicit timestepping. To maintain numerical convergence for large timesteps, the following convex energy splitting was applied to the double-well function $f(\xi) = f_c(\xi) + f_e(\xi)$:

$$f_c(\xi) = \frac{1}{16}(2\xi - 1)^4 \tag{29a}$$

$$f_e(\xi) = \frac{1}{16}(-8x^2 + 8x - 1) \tag{29b}$$

This choice of splitting is symmetric about $\xi = .5$ and importantly maintains the convexity requirement even outside of the rage $\xi = 0..1$, which helps with convergence for numerically stiff, heterogeneous simulations.

Results

Simulation results for the benchmark problem are shown in Fig. S15. The model reasonably captures the transitions in fractal dimension, gap-averaged saturation, and displacement efficiency, across the three injection rates and over most of the contact angles. However there is discrepancy for $\theta = 7°$, strong imbibition. This is likely because the displacement has become inhomogenous in the depth direction, and the depth-averaged model is inadequate. This could best be addressed by simulating the 3D pore structure with a Cahn-Hilliard-Brinkmann model, which would also enforce no-slip boundary conditions at the pore walls (the present model is surprisingly successful even though no-slip boundaries are not enforced). Finally, it might also be possible to use nonlinear relative permeability functions with a depth-averaged model to compensate for the lack of resolution in the depth dimension.
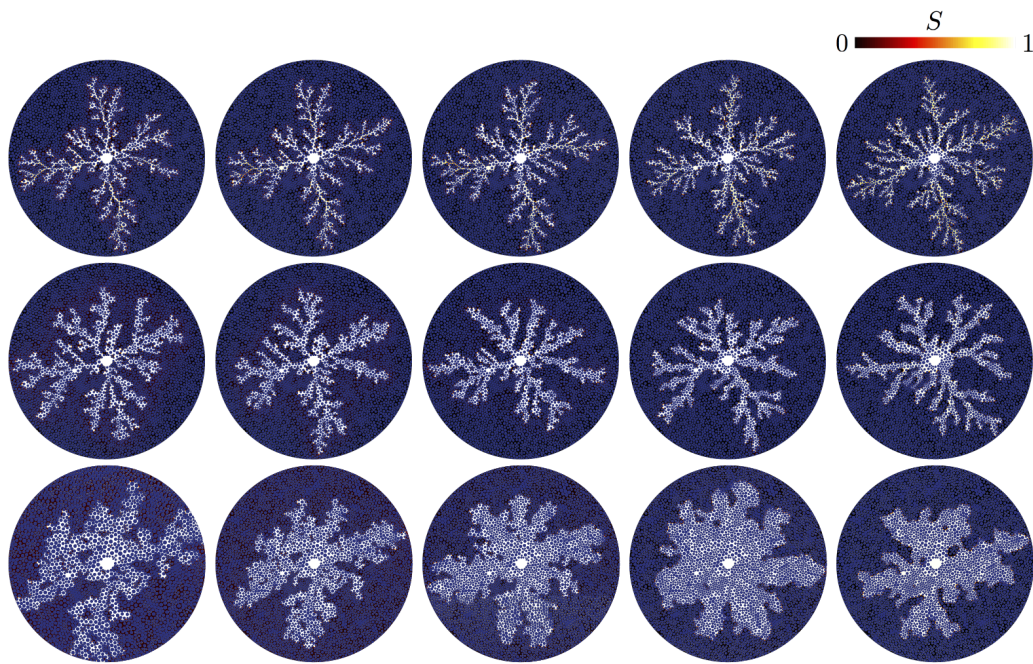
FIG. S15: Simulated displacement patterns for different wettability conditions (left to right: $\theta = 150°$, $\theta = 120°$, $\theta = 90°$, $\theta = 60°$, $\theta = 7°$) and capillary numbers (top to bottom: $\mathrm{Ca} = 2.9$, 2.9×10^{-1}, and 2.9×10^{-2}). The pore structure was discretized at a resolution of 2048×2048 pixels, which was enough to resolve the smallest pores.

Level-Set Model 1 (LS1)

Authors: Rahul Verma and Maša Prodanović
Email: masha@utexas.edu

Introduction

Level set methods are a broad class of methods for modeling interface movements, first proposed by Osher and Sethian in their seminal work [78]. The method has since been applied for a wide variety of applications: from image-processing and modeling flames to multiphase flows, and was introduced for modeling quasi-equilibrium fluid/fluid interface movement in porous media by Prodanović and Bryant [25], and subsequently extended for wettability modeling by Jettestuen *et al.* [26], and Verma *et al.* [27]. Since this is a quasi-static method, it was only intended for capillary-dominated, low capillary number flow conditions.

Model Description

The level set method is based on the main level set evolution equation:

$$\partial_t \phi + (a - b\kappa)|\nabla\phi| + \vec{V} \cdot \nabla\phi = 0 \tag{30}$$

The level set function ϕ is defined at each grid point throughout the domain of interest as the distance from the wetting/non-wetting fluid interface, which is the zero level set. ϕ is defined such that it is positive "outside", or on the side on convexity, and negative on the concave side. For instance, in a two-phase porous media formulation, $\phi > 0$ could denote the wetting phase, and $\phi < 0$ denotes the non-wetting phase and solid grain together (the choice of sign is, of course, arbitrary). As the interface advances, the ϕ function is updated throughout the domain according to the level set equation. Defining the interface implicitly means that changes in the topology of the fluid phases, such as snap-off and merging of fluid menisci, are handled automatically.

The term a is the speed of the interface normal to itself, while the curvature-dependent term $b\kappa$ acts opposite to the imposed normal speed a. b determines how strong the effect of curvature is and $\vec{V}$ represents the external advective field.

The level set method used here models capillary-dominated fluid flow by employing a variational technique: in the main pore space, the sum $a - b\kappa$ represents the difference between imposed capillary pressure (a) and the surface tension force ($b\kappa$) (reproducing the Young-Laplace equation), while near the boundaries, a, b and $\vec{V}$ are modified to impose contact angles. In the methodology introduced by Jettestuen *et al.* [26], this is achieved using a Heaviside function:

$$H(\psi) = \begin{cases} 0, & \psi < 0 \\ \frac{1}{2} + \frac{\psi}{2\epsilon} + \frac{1}{2\pi}sin\left(\frac{\pi\psi}{\epsilon}\right), & -\epsilon \leq \psi \leq \epsilon \\ 1, & \psi > \epsilon \end{cases} \tag{31}$$

The heaviside function takes a value of 1 where the level set is positive, and 0 where the level set is negative. Near the interface, it varies over a distance of $3\Delta x$, so that there are no sharp changes in the values. In addition, the level set needs to be reinitialized every few time steps to preserve the signed distance properties of the level set.

The equation proposed by Jettestuen *et al.* then becomes:

$$\begin{aligned} \phi_t + \{H(-\psi)\kappa_0 - S(\psi)H(\psi)cos\beta|\nabla\psi|\}|\nabla\phi| \\ + S(\psi)H(\psi)\nabla\psi \cdot \nabla\phi = H(-\psi)\kappa_\phi|\nabla\phi| \end{aligned} \tag{32}$$

with the the individual velocities given by:

$$a = (H(-\psi)\kappa_0 - S(\psi)H(\psi)cos\beta|\nabla\psi| \tag{33}$$

$$b = H(-\psi)\kappa_\phi \tag{34}$$

$$\vec{V} = S(\psi)H(\psi)\nabla\psi \tag{35}$$

New formulation for trapping

The method described up to now does not take trapping of phases into account. Jettestuen *et al.* and Verma *et al.* only focused on single-pore systems, and so could avoid this problem, but in modeling large systems with many pores, this cannot be ignored. Here, we introduce the concepts of modeling trapped phases using immobile "masks", one for the non-wetting phase, ψ_{nw}, and one for the wetting phase, ψ_w. So, every time the level set is reinitialized, it is checked for connectivity of both the wetting and the non-wetting phases. For this purpose, the level set first needs to be converted to a binary representation of 0s and 1s. Subsequently, a connectivity algorithm yields disconnected components for both the non-wetting and wetting phases, and the disconnected component masks are constructed. The masks need to be reconstructed from scratch each time, as merging and snap-off would change the connectivity of the disconnected phases.

The reconstructed masks can then be used to update the normal and curvature velocities, using the heaviside functions. For example, $H(-\psi_w)$ takes value of 1 where ψ_w is negative, and zero where it is positive. So, in the wetting trapped phase , $H(-\psi_w)$ is 0, and 1 in the main pore space. So we can update the normal and curvature velocities using this formulation:

$$a = H(-\psi_w)H(-\psi_{nw})(H(-\psi)\kappa_0 - S(\psi)H(\psi)cos\beta|\nabla\psi| \tag{36}$$

$$b = H(-\psi_w)H(-\psi_{nw})H(-\psi)\kappa_\phi \tag{37}$$

Note that the advective velocity term doesn't need to be updated, as it is only applied near the interface anyway. So inside the trapped phase, there is no reason to apply it. For more details please refer to the PhD thesis of Verma [28].

We apply this formulation to the experimental setup used by Zhao *et al.* to simulate fluid displacement for varying wettabilities in a micromodel. The original experimental geometry is provided as a set of 2D points, corresponding to disk centers, with accompanying radii information. Using this information, we reconstruct the domain. Since the domain is described analytically, we increased the resolution of the original experimental images to a limit where the computational costs for the level set method would not be too prohibitive. The eventual domain size we simulate is 4439x4439 pixels, with each pixel size 24.9 μm, compared to the experimental resolution of 54 μm. To save computational costs, we are ignoring the third dimension – in the experiment, this corresponds to a thickness of 100 μm. The level set results are shown in Figure S16.
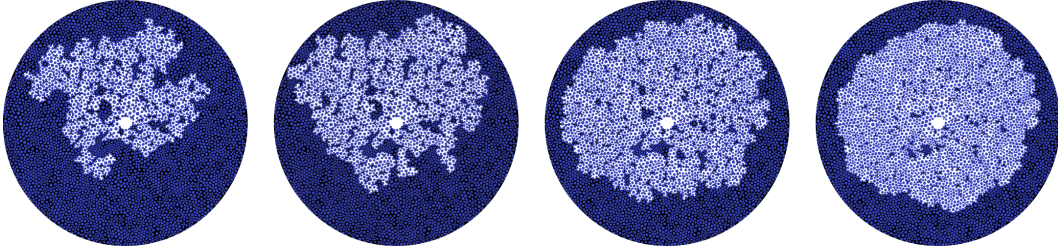

FIG. S16: Quasi-static simulations of the displacement patterns for different wettability conditions (left to right: $\theta = 150°$, $\theta = 120°$, $\theta = 90°$, $\theta = 60°$).

Volume-of-Fluid Method 1 (VF1)

Authors: Julien Maes, Sebastian Geiger
Email: j.maes@hw.ac.uk

Model Description

In the VOF method, the location of the interface is deduced from an indicator function α_1, which is equal to the volume fraction of fluid number 1 in each grid cells. For cells which are crossed by the interface, α_1 lies between 0 and 1. The indicator function for phase number 2 is defined as $\alpha_2 = 1 - \alpha_1$. The single-field velocity, pressure, density and viscosity are defined as

$$
\begin{aligned}
\mathbf{u} &= \alpha_1 \mathbf{u}_1 + \alpha_2 \mathbf{u}_2, \\
p &= \alpha_1 p_1 + \alpha_2 p_2, \\
\rho &= \alpha_1 \rho_1 + \alpha_2 \rho_2, \\
\mu &= \alpha_1 \mu_1 + \alpha_2 \mu_2.
\end{aligned}
\tag{38}
$$

The single-field velocity and pressure solve the single-field incompressible Navier-Stokes equations

$$
\begin{aligned}
\nabla \cdot \mathbf{u} &= 0, \\
\rho \left(\frac{\partial \mathbf{u}}{\partial t} + \mathbf{u} \cdot \nabla \mathbf{u} \right) &= -\nabla p + \nabla \cdot \boldsymbol{\tau} + \rho \mathbf{g} + \mathbf{f}_\gamma,
\end{aligned}
\tag{39}
$$

where $\boldsymbol{\tau}$ is the global stress tensor

$$
\boldsymbol{\tau} = \mu \left(\nabla \mathbf{u} + \nabla \mathbf{u}^T \right),
\tag{40}
$$

and $\mathbf{f}_\gamma$ is the surface tension force

$$
\mathbf{f}_\gamma = \gamma \kappa \mathbf{n}_{12} \delta_{12}.
\tag{41}
$$

Here δ_{12} is a Dirac function located on the interface. At the fluid-fluid-solid triple point, the interface intersects the normal of the solid surface at a contact angle θ such that

$$
\mathbf{n}_{12} = \cos\theta \mathbf{n}_s + \sin\theta \mathbf{t}_s,
\tag{42}
$$

where $\mathbf{n}_s$ and $\mathbf{t}_s$ are the normal and tangent vectors to the solid surface, respectively [79].

The indicator function solves the following transport equation

$$
\frac{\partial \alpha_1}{\partial t} + \nabla \cdot (\alpha_1 \mathbf{u}) + \nabla \cdot (\alpha_1 \alpha_2 \mathbf{u}_r) = 0,
\tag{43}
$$

where $\mathbf{u}_r = \mathbf{u}_1 - \mathbf{u}_2$ is the relative velocity. This advection equation is exact because its derivation does not include any assumption. It results from the volume averaging of the continuity equations (see Graveleau *et al.*, [80] for the derivation). Since it involves $\alpha_1 \alpha_2$, the second advection term has non-zero value only in the cells containing the fluid-fluid interface. However, there is no partial differential equation that governs the relative velocity. Therefore, $\mathbf{u}_r$ has to be modelled in order to close Eq. (43). To maintain a sharp interface, $\mathbf{u}_r$ is usually modelled as a compressive velocity $\mathbf{u}_c$ normal to the interface and with an amplitude based on the maximum of the single-field velocity [81]

$$
\mathbf{u}_r \equiv \mathbf{u}_c = \mathbf{n}_{12} \left[\min \left(\frac{|\phi|}{A_f}, \max_F \left(\frac{|\phi|}{A_f} \right) \right) \right],
\tag{44}
$$

where ϕ is the volumetric flux and A_f is the cell surface area.

The surface tension force acts only at the interface, which can be mathematically described as a surface. While using the Finite Volume method [82], the surface tension force cannot be computed as such and it must be approximated by a body

force. Brackbill *et al.*, 1992 [79] developed an approximation, referred to as Continuous Surface Force (CSF), where $\mathbf{n}_{12}\delta_{12}$ is approximated by $\nabla\alpha_1$ and κ by $\nabla \cdot \left(\frac{\nabla\alpha_1}{\|\nabla\alpha_1\|}\right)$. The surface tension force is then given by

$$\mathbf{f}_\gamma^{\text{CSF}} = \gamma\nabla \cdot \left(\frac{\nabla\alpha_1}{\|\nabla\alpha_1\|}\right)\nabla\alpha_1. \tag{45}$$

The VOF-CSF method is attractive because of its simplicity. However, Scardovelli & Zaleski, 1999 [83] reported the presence of spurious currents in the capillary dominated regime, which originates from errors in calculating the normal vector and the curvature of the interface. To limit the spurious currents, we use the Sharp Surface Force (SSF) method whereby the indicator function is smoothed by a Laplacian smoother for the computation of the curvature and sharpened by a curtail function for the computation of the surface tension force [84, 85]

$$\mathbf{f}_\gamma^{\text{SSF}} = \gamma\nabla \cdot \left(\frac{\nabla\hat{\alpha}_1}{\|\nabla\hat{\alpha}_1\|}\right)\nabla\tilde{\alpha}_1,$$

$$\hat{\alpha}_1 = C_{sK}\frac{\sum\alpha_{1f}A_f}{\sum A_f} + (1 - C_{sK})\,\alpha_1, \tag{46}$$

$$\tilde{\alpha}_1 = \frac{\left(\min\left(\max\left(\alpha_1, \frac{C_s}{2}\right), 1 - \frac{C_s}{2}\right) - \frac{C_s}{2}\right)}{1 - C_s},$$

where α_{1f} is the value of α_1 at the face centre calculated using linear interpolation, and C_{sK} and C_s are smoothing and sharpening constants. In this work, we use $C_{sK} = 0.1$ and $C_s = 0.1$. In order to eliminate some of the parasitic velocities that arise parallel to the interface, capillary forces parallel to interface are filtered [85]

$$f_{c,\text{filt}} = f_c - f_{\text{filt}}^{\text{old}},$$

$$\nabla \cdot \nabla p_c = \nabla f_{c,\text{filt}}, \tag{47}$$

$$f_{\text{filt}} = \frac{\delta_{pc}}{\delta_{pc} + \epsilon}\left(f_{\text{filt}}^{\text{old}} + c_{f_{c,\text{filt}}}\langle\nabla p_c - (\nabla p_c \cdot n_I)\,n_I\rangle_{c\to f}\,n_I\right).$$

The constant $c_{f_{c,\text{filt}}}$ is set to 0.01 to avoid capillary pressure build-ups and velocity bursts [29]. In addition, the capillary fluxes are also filtered based on zero-net capillary force constraints

$$\phi_c = \int\int (f_{c,\text{filt}} - \nabla p_c) \cdot n_f,$$

$$\phi_{c,\text{filt}} = \phi_c - \min\left(\max\left(\phi_c, \phi_{c,\text{thresh}}\right), -\phi_{c,\text{thresh}}\right), \tag{48}$$

$$\phi_{c,thresh} = c_{\phi_c,\text{filt}}\,|f_{c,\text{filt}}|_{\text{avg}}\,|A_f|.$$

This correction eliminates capillary fluxes when they are in the range of numerical errors [85].

Numerical implementation

The mathematical model formed by Eq. (39) and Eq. (43) is implemented in the open source Computational Fluids Dynamics toolbox OpenFOAM (`www.OpenFOAM.org`) as an internal VOF solver called *interFoam*. *interFoam* solves the system on a collocated Eulerian grid with a predictor-corrector strategy based on the Pressure Implicit Splitting Operator (PISO) algorithm [86]. An semi-implicit formulation is used to treat the coupling between the phase distribution equation (Eq. (43)) and the NSE equation (Eq. (39)) with a fixed number of iterations (nOuterCorrectors). The space discretization of the convection term $\nabla.(\alpha 1 u)$ and compression term $\nabla \cdot (\alpha_1\alpha_2 u_r)$ is performed using the second-order *van Leer* scheme [87]. The standard *interFoam* solver has been modified to include the SSF formulation (Eq. (46)).

Geometry and grid

To mesh the computational domain, a 2D uniform Cartesian grid comprising 1250×1250 grid blocks is generated. Then, all cells containing the solid posts are removed and replaced by rectangular and triangular cells that match the solid boundaries using the OpenFoam snappyHexMesh utility (Fig. S17). The final grid contains 657694 cells. For low Ca simulations, the geometry has been truncated from the original image and the outlet is situated at a radius of 3 cm. In this case, the final grid contains 251542 cells. All simulations are performed with a constant time-step $\delta t = 2 \times 10^{-4}$ s. We use 3 iterations of the PISO loop and 2 iterations of the semi-implicit loop (nOuterCorrectors).
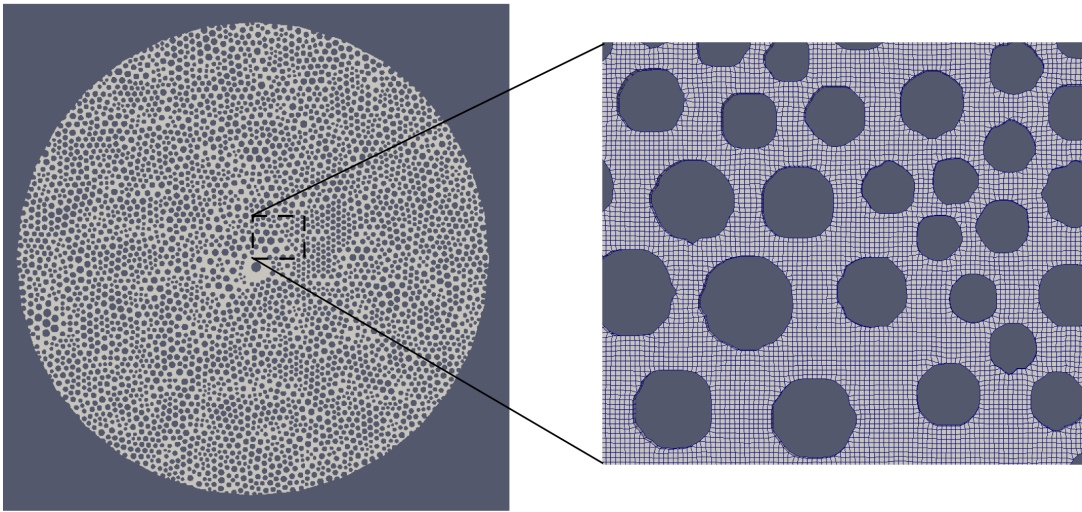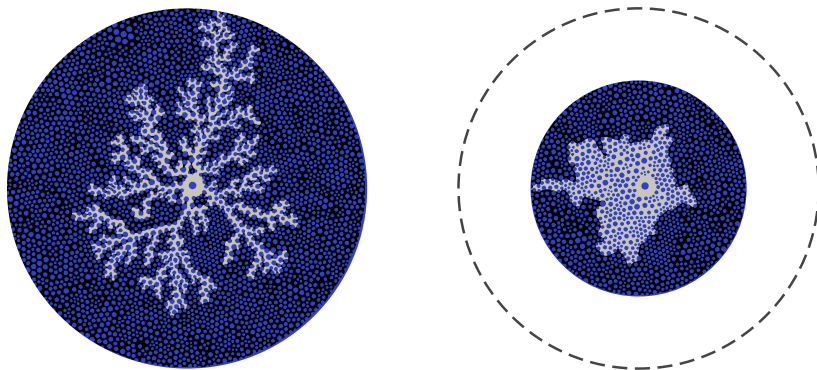
FIG. S17: Pore geometry and boundary conditions.

FIG. S18: Simulated fluid-fluid displacement pattern for strong drainage at high Ca (left) and weak imbibition at low Ca (right).

Pore-network Model 1 (PN1)

Authors: Morten Vassvik, Alex Hansen
Email: Alex.Hansen@ntnu.no

Introduction
Our model is a single-pressure dynamic pore-network model for incompressible two-phase flow in porous media, based on the earlier work of Aker *et al.* [31] and Knudsen *et al.* [32].

Model Description
The network is defined as a graph of connected links and nodes. Each node corresponds to the center of a pore-body, and each link corresponds to a pore-throat in addition to part of adjacent pore-bodies. The links carry all the pore volume, and the nodes have no volume.

Each link can hold up to two fluids simultaneously, represented as bubbles that are spaced out along the link length. Depending on the shape of each link and the distribution of fluids inside each link, we relate the volumetric flow rate going through the link at a given time to the pressure gradient across the link through a traditional Hagen–Poiseuille-type relationship. For single phase, this can be stated as

$$q = -\frac{k(x)A(x)}{\mu}\frac{\mathrm{d}p}{\mathrm{d}x},\tag{49}$$

where k is the *local permeability*, A is the cross-sectional area, μ is the viscosity, and p is the pressure. Each quantity can in principle be regarded as function of position x, so that we can account for variations along the link length. The flow rate q has to be the same for any position along the link due to the incompressibility of the fluids.

In order to obtain an expression for the link flow rate as a a function of the pressure difference between the two nodes it connects, we integrate Eq. (49), resulting in

$$p(x_2) - p(x_1) = -q\mu \int_{x_1}^{x_2} \frac{\mathrm{d}x}{k(x)A(x)},\tag{50}$$

where x_1 and x_2 are two arbitrary positions along the link. We can simplify this expression by non-dimensionalizing the integral,

$$\int_{x_1}^{x_2} \frac{\mathrm{d}x}{k(x)A(x)} = \frac{1}{\kappa_0} \int_{x_1}^{x_2} \frac{\kappa_0 \mathrm{d}x}{k(x)A(x)},\tag{51}$$

where the factor κ_0 (units m^3) is defined by

$$\kappa_0^{-1} = \int_0^L \frac{\mathrm{d}x}{k(x)A(x)},\tag{52}$$

which encodes the effect of permeability k, the cross-sectional area A and the length L on the mobility. We can then write Eq. (50) as

$$p(x_2) - p(x_1) = -\frac{q\mu}{\kappa_0}I(x_1, x_2),\tag{53}$$

where we have defined the integral

$$I(x_1, x_2) = \int_{x_1}^{x_2} \frac{\kappa_0 \mathrm{d}x}{k(x)A(x)}.\tag{54}$$

which serves as a weighting function, with the property that $I(0, L) = 1$.

If we have have two immiscible fluids inside a link, separated by an interface, we can use Eq. (53) for each phase separately and add up their contribution to get a relationship between the flow rate q and the pressure difference across the entire link Δp, where Δp is defined as the difference in pressure in the nodes that the link connects. Any jump in pressure across interfaces (due to surface tension) is accounted for by an additional capillary pressure difference. For example, if we have a link containing a wetting fluid followed by a non-wetting fluid whose menisci are at position x, then we would end up with,

$$q = -\frac{\kappa_0}{\mu_{\text{eff}}}\left(\Delta p - p_c\right), \tag{55}$$

where $\mu_{\text{eff}} = \mu_{\text{nw}}I(0,x) + \mu_{\text{w}}I(x,L)$ and $p_c = p(x^+) - p(x^-)$. This formulation allows for the wetting angle θ to vary as a function of position along the wall, and to account for a dynamic contact angle, but in the present work we keep these constant.

It should be noted that Eq. (55) and (49) reduces to the familiar Hagen–Poiseuille relation when we assume a straight tube, where $k = r^2/8$, $A = \pi r^2$ and r is the radius of the tube.

Mass conservation at each node (*i.t.* flow rate in equals flow rate out) results in a linear system of equations for the node pressures, whose coefficients are functions of adjacent link mobilities and capillary pressures. By solving this system using the appropriate boundary conditions we can use Eq. (55) to calculate the flow rate in each link, which in turn can be used to evolve our system in time by displacing any menisci inside each link. Any fluid that has exited a link is immediately distributed into neighbouring links.

Application: Microfluidic Flow Cell

The equations introduced in the previous section are generic in nature, as we made no specific comment on the exact geometric dependencies of k, A and p_c. In the following we will motivate the exact expressions used based on the experimental setup of Zhao *et al.* [2].
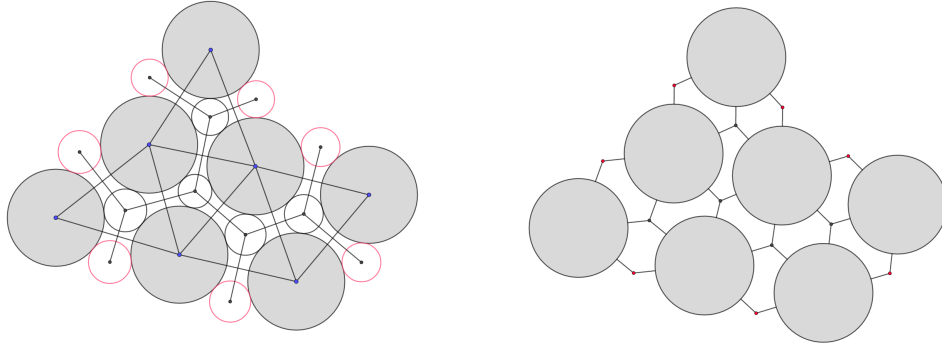

FIG. S19: Left: The figure shows how a set of posts can be triangulated to create a pore-network. Boundary nodes (in red) are created by mirroring a node across the boundary edge. Right: The figure shows the partitioning of the pore space into links and nodes.

Given a microfluidic flow cell patterned with posts, our goal is to extract a pore-network representing the void space. We start by triangulating the set of post positions, which yields a triangular partitioning of the void space, where the vertices of each triangle corresponds to a post center. For each triplet of points in the triangulation we can fit a fourth virtual post such that it exactly touches all three posts simultaneously. The center of this post defines the nodes in our network, corresponding to the center of a pore-body. Adjacent nodes are then connected based on neighbouring triangles in the triangulation, giving us a set of links. Along the boundary (inlets and outlets) we create new inlet and outlet nodes by mirroring adjacent nodes across the boundary triangle edges. The nodes and links together make up the pore-network as illustrated in Fig. S19.

The nodes are considered as single points and they hold no volume. We partition the pore space such that a pore-body is distributed among adjacent links as illustrated in Fig. S19.

For each link we can now calculate, or at least approximate, the constant term κ_0 and the position-dependent weighting function $I(a,b)$ introduced in the previous section. The cross-sectional area is $A(x) = hw(x)$, where h is the height of the cell, and $w(x)$ is the variable width as we move along a link. We model the local permeability k based on flow through a rectangular pipe [88]

$$k = \frac{hw}{12}\left[\frac{1}{\gamma} - \frac{6}{\gamma^2}\sum_{n\,\text{odd}}\frac{\tanh(a_n\gamma)}{a_n^5}\right], a_n = \frac{n\pi}{2}, \tag{56}$$

where $\gamma = w/h$ is the local aspect ratio. In practice we truncate the series in Eq. (56) after 10 terms, which is sufficient for the aspect ratios in this case.

The menisci separating the two phases are modelled as circular arcs that meet the posts at a specified wetting angle. By moving a circular arc along a link we can map out the capillary pressure difference as a function of position on a per-link bases. This is illustrated in Fig. S20, for both an advancing and receding menisci. For completely wetting system the capillary pressure is simply given by the inverse of the radius of curvature of such an arc. For intermediate wetting angles we use the formula

$$p_c(x, \theta) = \frac{\gamma}{r(x)} \cos\left[\theta - \cos^{-1}\left(\frac{r(x)}{R(x)}\right)\right] + \frac{\gamma}{h}\cos\theta, \tag{57}$$

where $r(x) = w(x)/2$ is half the distance between the points where the menisci meets the post walls and R is the radius of curvature of the fitted arc. In the special cases of $\theta = 0°$ and $\theta = 180°$, the first term reduces to $p_c(x) = \pm\frac{\gamma}{R(x)}$, as required. Function (57) is plotted in Fig. S20 for different wetting angles.
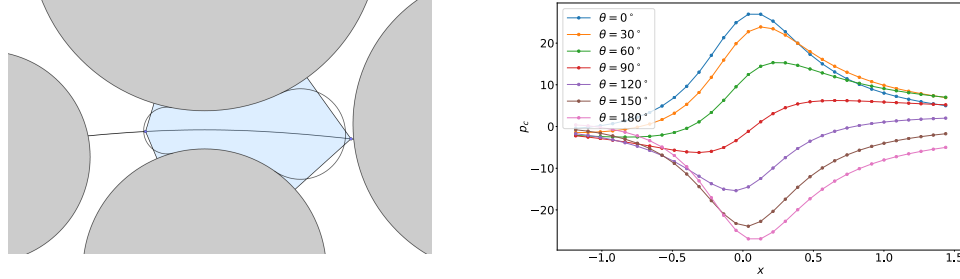

FIG. S20: Left: The figure illustrates a non-wetting bubble inside a link (represented by the solid line). Each menisci along the link is represented by a solid circle segments. The circular segments are placed such that the volume bounded by the circular segments is the same as the shaded blue area. Right: The figure shows the capillary pressure as a function of position and wetting angle.

General Comment

Using Eq. (56) we measure a single-phase (oil-filled) global pressure difference of 28816 Pa for the largest reported capillary number. Note that the pressure is measured at the outer edges of the injection area, at a distance 3 mm away from the injection point on average. This measurement is consistent with the measured pressure difference reported in Zhao *et al.* [2] when extrapolated to the injection point where the pump sits.

For our simulations, the structures observed appear consistent with experiments for high flow rates, but the simulations do not reproduce the same structures for low capillary numbers. In particular, the co-operative effects for the neutral and weak imbibition cases are not reproduced. This is most likely due to the functional expression we used for the capillary pressures: even for the neutral and weak imbibition regimes there is still a capillary barrier present, as can be seen in Fig. S20. This together with our choice of boundary conditions results in an invasion percolation type behavior for all wettabilities, with the main difference being that narrow cross-sections are preferred in the neutral and weak imbibition cases.

Neglecting film and corner flows might also have a big impact on this, but the displacement patterns of the experiments do not appear to be dominated by corner flow and film transport except in the strong imbibition regime. It might be possible to incorporate these effects into the capillary pressure term in the future.
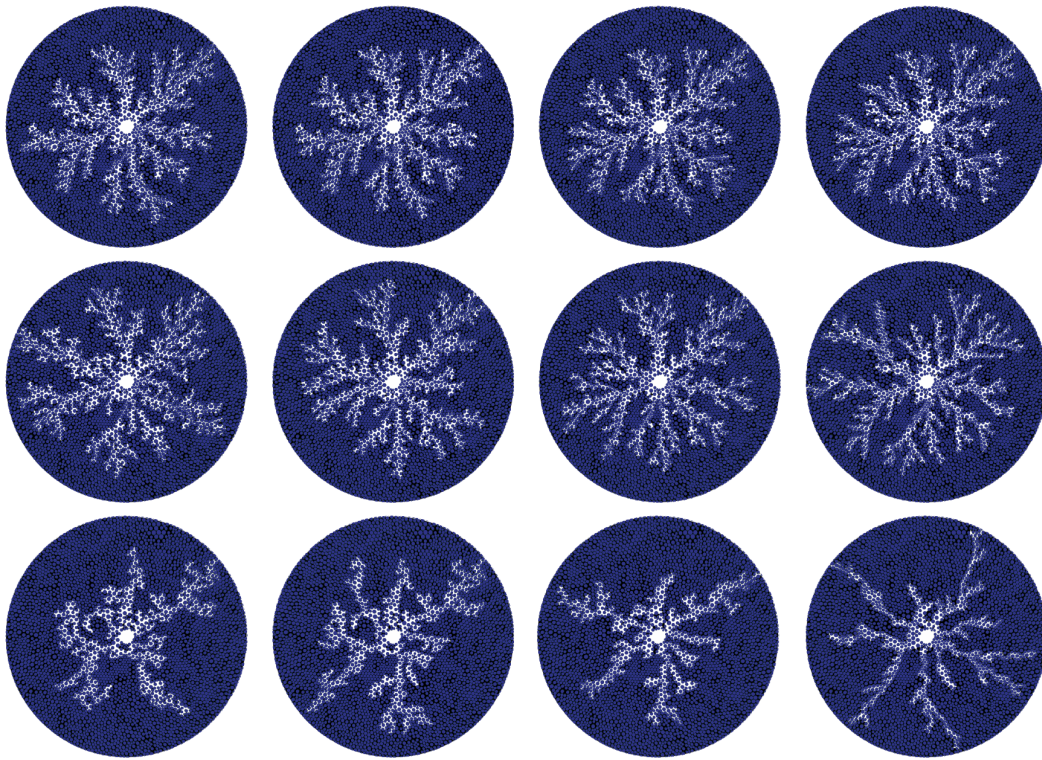
FIG. S21: Simulated displacement patterns for different wettability conditions (left to right: $\theta = 150°$, $\theta = 120°$, $\theta = 90°$, and $\theta = 60°$) and capillary numbers (top to bottom: $\mathrm{Ca} = 3.2$, 3.2×10^{-1}, and 3.2×10^{-2}).

Pore-network Model 2 (PN2)

Authors: Enrico Segre, Ran Holtzman
Email: enrico.segre@weizmann.ac.il, holtzman.ran@mail.huji.ac.il

Introduction

We extended the model presented in Holtzman & Segre, 2015 [33] by including an arbitrary distribution of cylindric posts. The resulting model combines the quasistatic approach originally proposed by Cieplak & Robbins, 1990 [45] with a single pressure, dynamic model of flow through the pore network, in which the interface motion is not resolved below the pore scale. Each triplet of posts (identified by Delaunay triangulation) defines a pore, which is connected to three neighbours via throats. The throats are the gaps between each pair of the three posts associated with a given pore. The resistance to flow at a given throat is given by its width w and filling state. The fluid-fluid interface is represented as a set of cylindric menisci, which touch the posts at an in-plane contact angle θ. The fluid-fluid interface has a radius of curvature $R = \gamma/\Delta p$, where Δp is the local pressure jump across the meniscus. Given R and θ, the position and hence stability of each meniscus can be solved analytically. The evolving resistances of the throats determine the pressure field. Our model is effectively 2D in the sense that we only consider the in-plane curvature $R = R_{\text{in}}$ in computing the radius of curvature. This approximation is reasonable for 3D porous media when the in-plane curavature is much larger than the out-of-plane curvature $R_{\text{in}} \ll R_{\text{out}}$, which corresponds to the case where post diameters are much smaller than their height $d \ll h$. Despite this being at odds with the experimental setup of Zhao *et al.*, 2016 [2], our numerical results matched the experiment better when curvature correction to account for the finite height was neglected. Our model's resolution is at the level of the pore, and its bidimensionality does not capture the effects of film or corner flow, therefore limiting its ability to reproduce cases where these mechanisms become important, particularly in strong imbibition. However, the simplicity of our model results in a very efficent code that is capable of full-scale simulations in CPU times on the order of a minute. This feature allows large batch of simulations to be performed for the purposes of statistics, parametric exploration, and sensitivity analysis.

Model Description

The sample geometry is based on the post sizes and coordinates provided in the benchmark dataset. For the fluid properties we used the values given in Zhao *et al.*, 2016 [2]: $\eta_{\text{oil}} = 0.340\,\text{Pa} \cdot \text{s}$, $\eta_{\text{water}} = 0.99\,\text{mPa} \cdot \text{s}$, $\gamma = 13\,\text{mN/m}$. At each simulation step, the pressure field is computed across the whole network. Specifically, throats with stable menisci are considered impervious; a fixed resistance proportional to η_{oil} or η_{water} and w^{-3} (for a width w) is assigned to throats connecting pores occupied by the same fluid; whereas a variable resistance proportional to the downstream filling value is given to throats leading to incipiently invaded pores. The existing menisci are then tested for three types of instabilities [45]: (1) *burst*, when the curvature exceeds a threshold set by the local geometry; (2) *touch*, when a meniscus intersects a third, downstream post; and (3) *overlap* of adjacent menisci, destabilizing each other. The latter describes nonlocal, cooperative pore-filling, which smooths the interface. Overlaps are strongly affected by the contact angle, and hence are crucial in capturing wettability effects.
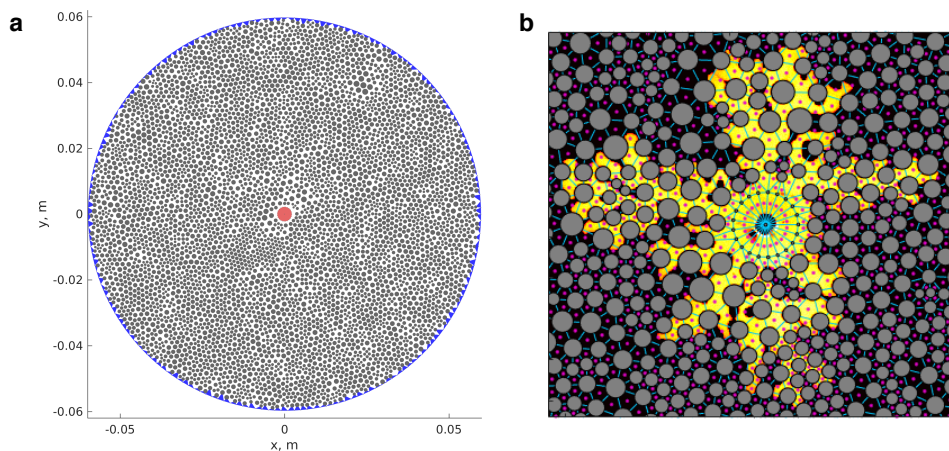

FIG. S22: (a) Model geometry. A fixed driving pressure P is assigned to the injection zone pores (in red) against zero pressure at the boundary pores (in blue). (b) Sampling of the experimental image, to derive pore occupancies to be used as numerical initial conditions. The greyscale image is sampled at the center (purple dot) of each pore (bounded by blue lines) confined by three neighbouring posts (grey circles).

Once a meniscus is destabilized, it invades the downstream pore at a rate calculated from the throat's viscous resistance by solving mass balance for the two incompressible immiscible fluids. Our model associates a filling value between 0 and 1 to each pore, without resolving the spatial distribution of the fluids *within* the pore. Pores downstream of destabilized menisci fill in parallel, and complete filling in different times, proportional to the pore volumes and local flow rates.

To enforce boundary conditions we added two sets of auxiliary posts to the given post distribution: (i) 21 posts along an inner circumference of radius 2.2mm; (ii) 380 posts along an external circumference of radius 59.7mm (see Fig. S22a). A nominal radius of 100 μm was assigned to the auxiliary posts. We enforce quasi-constant flow rate by imposing an arificially high hydraulic resistance in the inlet zone (Fig. S22a), such that most of the pressure drop occurs in the "buffer zone", making the flow resistance and hence pressure gradient across the porous sample insensitive to the evolving invasion pattern. By implementing the numerical "buffer zone", we achieve desired fixed flow rates of 2, 20, and 200 μL/min to within 5% accuracy by setting fixed pressures (*i.e.* Dirichlet boundary condition) at the inlet and outlet pores.

The experimental images show that the initial growth of the injection bubble is highly asymmetric. Since this could strongly affect the evolution of the pattern, we test its effect by comparing simulations with (i) symmetric initial conditions (starting with a completely water-filled inlet zone) vs. (ii) pore occupancy derived from experimental images at early stages, with different grayscale thresholds (Fig. S22b).

The simulation achieves breakthrough (with corresponding breakthrough time t_b) when a boundary pore is first invaded (Fig. S22a). By solving the pore-network pressure-flow system, our model tracks the total amount of fluid displaced during the simulation. We define E_d as the ratio between the amount of displaced fluid and the total pore volume. We take the mean filling value of all partially or totally invaded pores as the average saturation S. The fractal dimension D_f is computed by applying a threshold of $S = 0.01$ to the simulation result at breakthrough, rasterizing it on a $1000{\times}1000$ frame, and analyzing the resulting pattern with a box-counting algorithm [89].
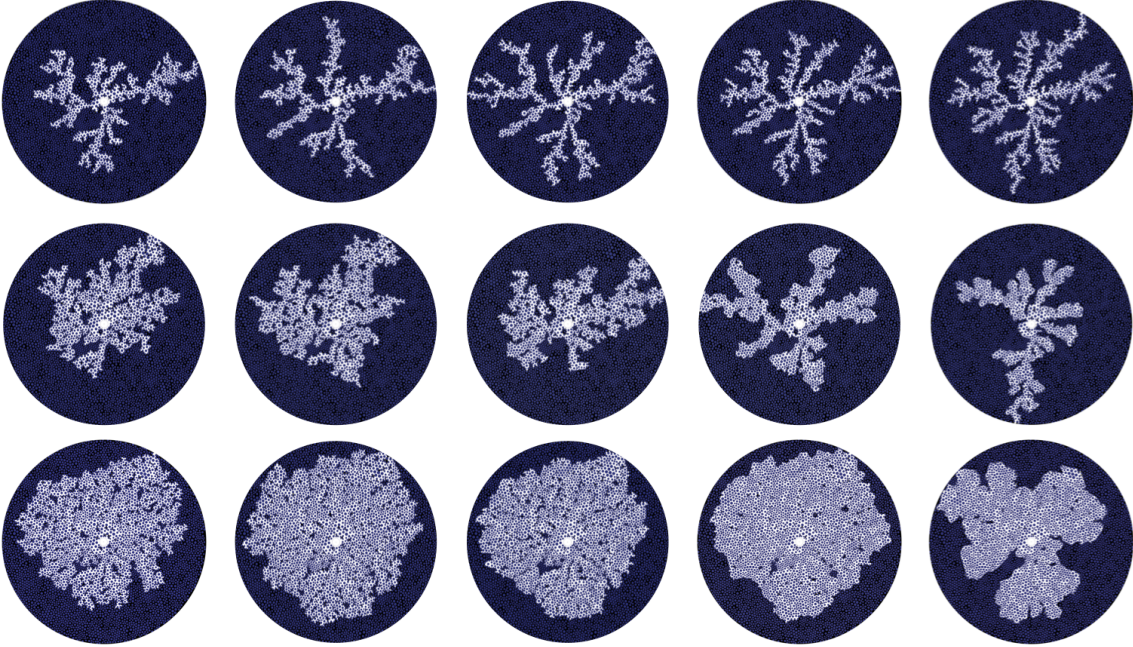

FIG. S23: Simulated displacement patterns for different wettability conditions (left to right: $\theta = 150°$, $\theta = 120°$, $\theta = 90°$, $\theta = 60°$, $\theta = 7°$) and capillary numbers (top to bottom: Ca = 2.9, 2.9×10^{-1}, and 2.9×10^{-2}), using initial conditions derived from experimental images. The *effective advancing* angle θ is measured through the wetting fluid (i.e. $\theta > 90°$ for drainage), as in Zhao *et al.* [2].
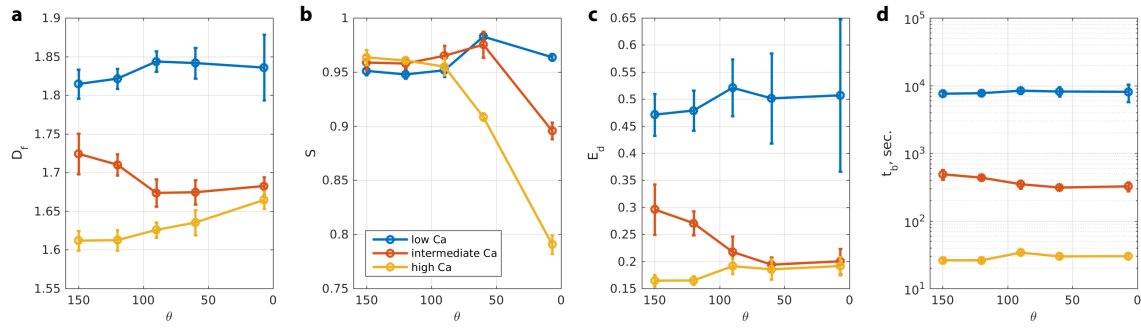
FIG. S24: Mean and standard deviation of the quantitative measures of five simulations for each wettability and capillary number, obtained with different values of control parameters and inital conditions. (a) Fractal dimension D_f. (b) Average saturation S – the mean filling value of all partially or totally invaded pores. (c) Displacement efficiency E_d – the ratio between the amount of displaced fluid and the total pore volume. (d) Breakthrough time t_b.

Pore-network Model 3 (PN3)

Authors: Bauyrzhan K Primkulov, Benzhong Zhao, Christopher W. MacMinn, and Ruben Juanes
Email: juanes@mit.edu

Introduction

We model fluid-fluid displacement in the flow cell with two approaches: a quasi-static model and a dynamic model. Each model features a range of validity for capillary numbers (Ca) and contact angles (θ).

The quasi-static network model [35] was designed for 2D micromodels in the limit of very small Ca, where we take advantage of the following conditions: (i) pressures are spatially uniform within invading and defending fluids; (ii) at a given pressure difference between invading and defending fluids, all local fluid-fluid interfaces between posts have the same curvature. Therefore, we can advance the invading fluid front in a manner of invasion-percolation [90], where the invading fluid always enters pores with lowest entry pressures. In particular, we explicitly calculate the critical pressures for pore-scale invasion events of Cieplak and Robbins [45, 91] as well as the corner-flow invasion events. As a result, the invading fluid front advances through single-pore piston-type displacement, cooperative pore filling, or corner-flow.

The dynamic moving-capacitor network model [36] relies on establishing an analogy between electric circuits and fluid-fluid displacement in porous media. The viscous pressure drop throughout the flow cell is captured by means of a network of resistors, while in-plane/out-of-plane components of the Laplace pressure are represented with moving capacitors/batteries at the invading fluid front.

Model Description – Quasi-static Model

Consider the local fluid-fluid interface between the two posts in Figure S25a. The shape of this interface is uniquely defined by its radius of curvature r_p and the contact angles at which it intersects the two posts [35]. When the pressure of the invading fluid increases, the interface moves forward while the radius of its curvature decreases. At some point, the local fluid-fluid interface reaches its last stable configuration. If the invading fluid pressure increases further, the interface becomes unstable and it advances (Figure S25b). We refer to this event as "burst". When a "burst" event takes place, the unstable local interface is replaced by two new ones with the nearest post.

The local fluid-fluid interface may become unstable before reaching the "burst" pressure. The "touch" event takes place when the interface touches the nearby post (Figure S25c) before reaching the "burst" pressure. The unstable interface between posts 1 and 2 is replaced by two new ones, connecting posts 1-3 and posts 3-2 in Figure S25c.

Another pore-scale event that may take place is "overlap". The "overlap" event occurs when two neighbouring interfaces coalesce inside the pore space (Figure S25d). Then the two interfaces between posts 1-2 and 2-3 are replaced by a single interface between posts 1-3.

Finally, a "corner-flow" event may take place when $\theta < 45°$. In strong imbibition, the invading fluid preferentially wets the corners between the posts and top/bottom plates (Figure S25e-f). As the pressure of the invading fluid increases, the corner menisci swell until one of the neighbouring posts is touched. This results in the advance of the invading fluid through a chain coating of the posts.

We explicitly calculate the critical pressures for all pore-scale events shown in Figure S25 [35]. Thus, we model the quasi-static invasion of the fluid-fluid interface in a manner of invasion-percolation, where the order of pore invasion is governed by the critical event pressures; pores with lowest critical pressures are invaded first. Different events are prevalent at different wettability conditions: (i) "burst" events dominate in strong drainage ($\theta > 145°$), and the invading fluid advances through capillary invasion; (ii) "touch" and "overlap" events dominate in weak imbibition ($75° > \theta > 45°$), where the invasion pattern grows through cooperative pore filling; (iii) "corner-flow" events are most frequent in strong imbibition ($\theta < 45°$), where the pattern grows through chain coating of the posts.

Model Description – Dynamic Model

Consider the analogy between the fluid-fluid displacement and an electric circuit. As the invading fluid is injected into the pore structure, three components of the pressure contrast emerge: (i) pressure gradient due to viscous dissipation, (ii) out-of-plane component (iii) and in-plane component of the Laplace pressure. This is equivalent to having an electric current through a circuit of resistors, batteries, and capacitors. The viscous pressure drop through the network can be calculated considering Poiseuille flow through the network of capillary tubes along with conservation of mass. This is equivalent to resolving the Ohm's law and Kirchhoff's current law in the network of resistors. The out-of-plane contribution to the Laplace pressure can be represented with batteries at the invasion front. These batteries introduce a discrete potential (pressure) increase or drop, depending on the contact angle θ between the fluid-fluid interface and the top/bottom plates of the flow cell. Finally, the in-plane contribution to the Laplace pressure can be represented through capacitors at the invading front. Here, electric potential (pressure) drop across the capacitor plates builds up with current (flow) until a threshold potential (critical pressure) is reached. If the potential
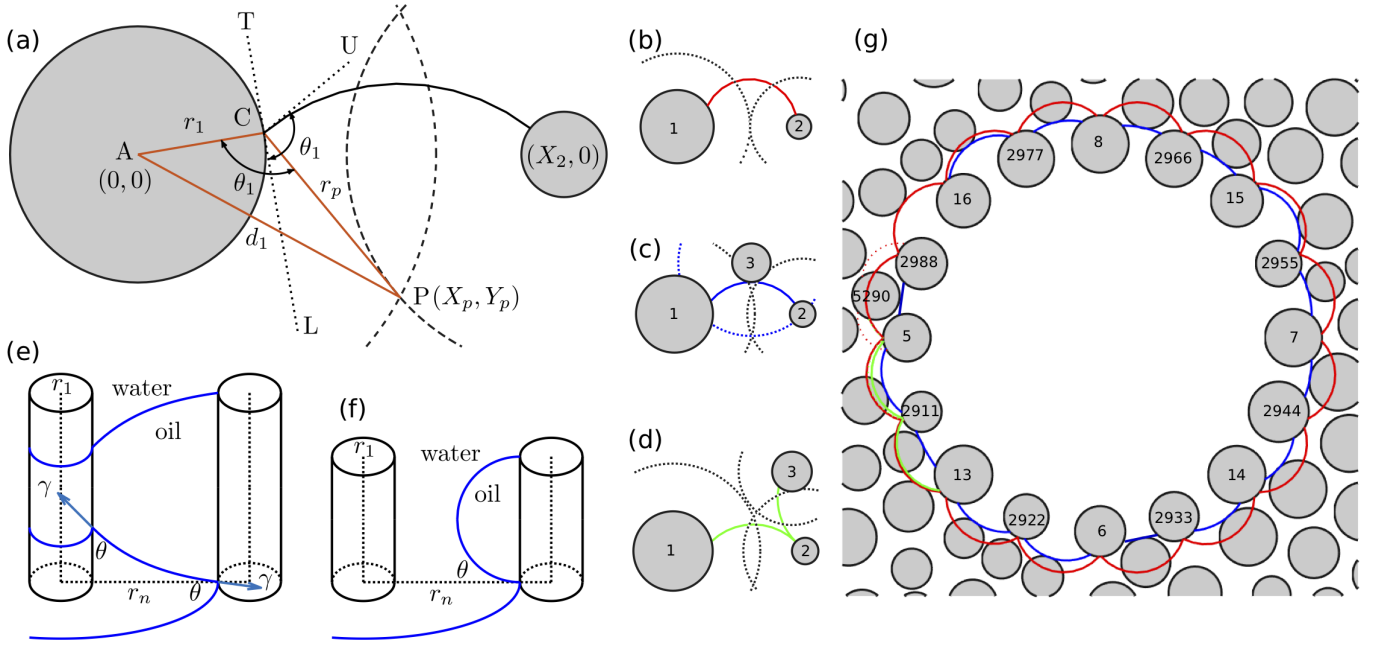
FIG. S25: Figure adapted from Primkulov *et al.* [35]. (a) Invasion front configuration between two posts; (b) Burst event: unstable interface (red line) advances into the pore; (c) Touch event: interface touches the nearest post; (d) Overlap event: two fronts (green lines) coalesce on post surface and fill the pore; (e) Corner-flow event: corner meniscus touches and coats the neighbouring post; (f) Capillary bridge event: corner menisci coalesce mid-post before reaching the next post; (g) Invading front configuration with post IDs: red, blue, green interfaces correspond to "burst", "touch", "overlap" critical interfaces.

increases above this threshold, the capacitor undergoes dielectric breakdown. In contrast, in its fluid counterpart, the capacitor moves to a new location ahead of the invading front following the rules of Cieplak and Robbins [45, 91] and restarts building up Laplace pressure.

Our formulation of the quasi-static invasion model gives us a-priory knowledge of these critical pressures. We use them as thresholds of the capacitors at the interface, such that filling of the capillary tubes with the invading fluid coincides with the local in-plane Laplace pressure thresholds. The effect of wettability in our model is captured through "burst", "touch" and "overlap" pore invasion events described earlier [35, 45, 91], whose relative frequency is a function of the contact angle θ.
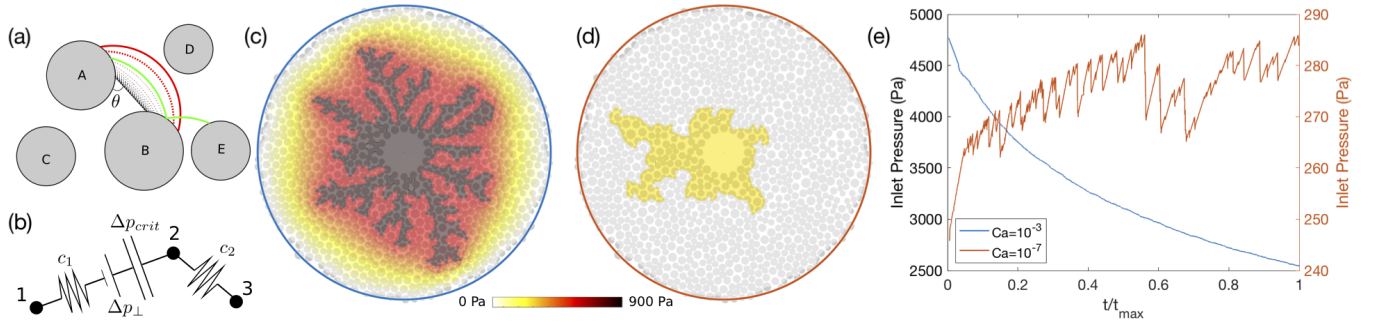

FIG. S26: Figure adapted from Primkulov *et al.* [36]. (a) Schematic diagram of the fluid-fluid interface motion in the 2D pore space. Dotted lines represent the interface at increasing pressures, where red and green stand for "burst" and "overlap" events respectively [45, 91]. (b) Electric analog of the pore space, where resistors, batteries and capacitors are responsible for viscous and Laplace pressure drops, respectively. Nodes 1, 2, 3 stand for pores ABC, ABD, BDE. (c) Final invasion pattern and spatial pressure profile for $Ca = 10^{-3}$ and $\theta = 160°$ (d) Uniform spatial pressure profile for $Ca = 10^{-7}$ and $\theta = 160°$ (e) Temporal pressure profiles at the injection pore bear close resemblance to experiments at low and high Ca [2, 92].

This framework allows capturing fluid-fluid displacement regimes at both high and low Ca. At high Ca, viscous forces dominate the dynamics, and large pressure gradients build up across the more-viscous defending fluid (Figure S26c). This results in the decreasing trend of the injection pressure with time (Figure S26e): as the fingers approach the outer boundary,
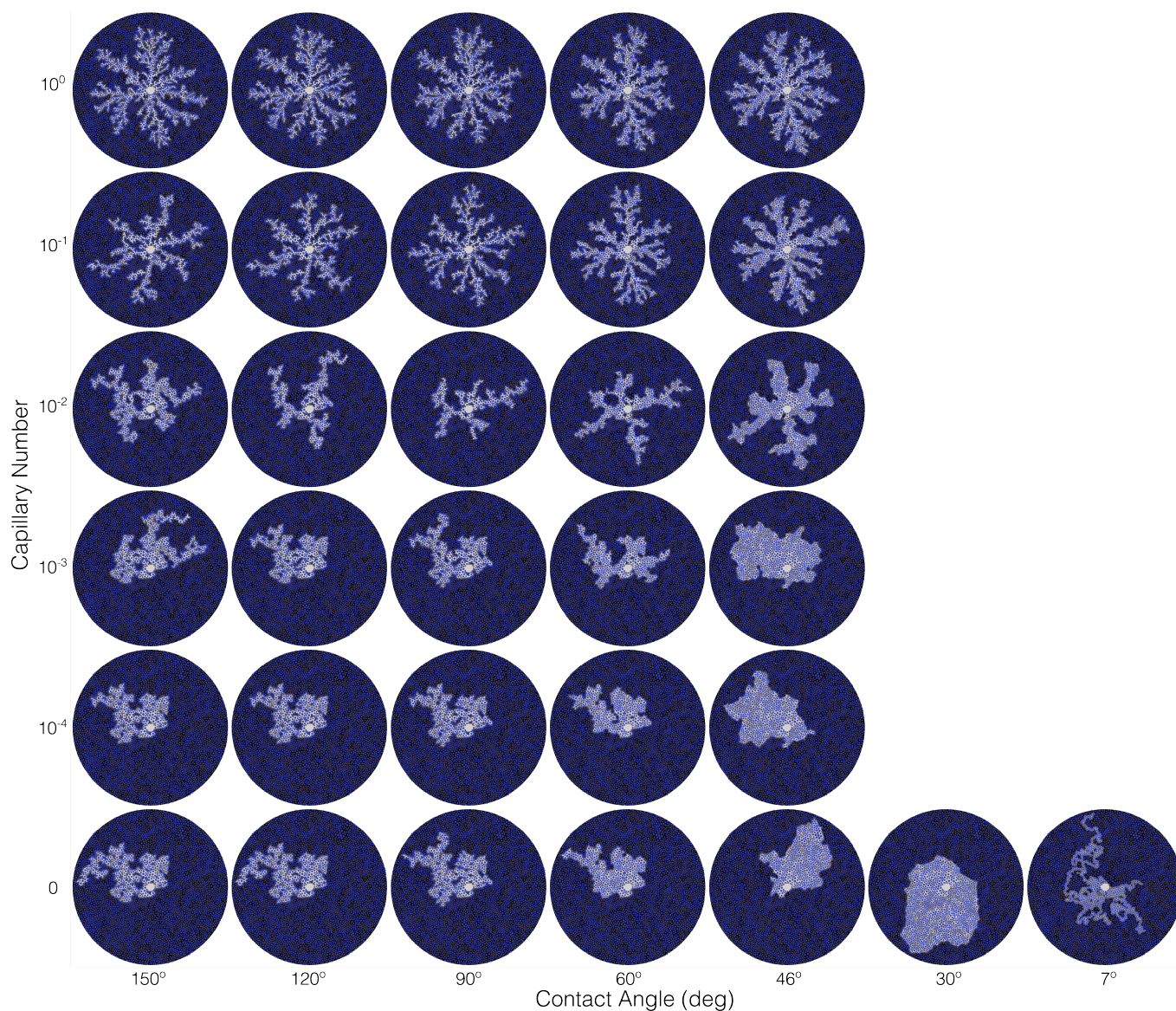
FIG. S27: Simulated displacement patterns for different wettability and capillary number conditions. The dynamic simulations (Ca > 0) were obtained using the dynamic moving-capacitor pore-network invasion algorithm [36]. The bottom row (Ca = 0) was generated with the quasi-static invasion algorithm [35].

smaller pressure drop across the flow cell is needed to maintain the prescribed flow rate. At low Ca, the pressure changes within the system come almost exclusively from the Laplace pressures at the invading front. This results in spatially uniform distributions of pressure in the invading and defending fluids (Figure S26d), and also in an intermittent profile of injection pressure as a function of time (Figure S26e).

Pore-network Model 4 (PN4)

Authors: Zhibing Yang
Email: zbyang@whu.edu.cn

Introduction
The two-dimensional modelling approach described here is similar to the pore-network model of Lenormand *et al.*, 1988 [93]. The pressure distribution is solved in both fluid phases. Fluid invasion and interface advancement are computed in discrete steps. However, we do not extract pore bodies and throats from the post locations of the micromodel. Instead, we discretize the pore space into smaller elements. The capillary resistance for each element is calculated based on the vertical gap between top and bottom walls and the horizontal gap between posts. Films and corner flows are not considered. Only the strong drainage condition (*i.e.* $\theta = 150°$) is simulated.

Model Description
The two-dimensional pressure distribution in the pore space is solved via a finite volume scheme, taking into account the capillary pressure jump at the fluid–fluid interface. The viscosity of the invading and the defending fluids are μ_{inv} and μ_{def}, respectively. Darcy's law is assumed valid locally. The flow rate q across the connection between two elements [for example, (i, j) and (i, j+1)] is given by the conductance C of the connection and the pressure drop between two neighbouring elements if no fluid–fluid interface or capillary pressure is involved:

$$q_{i,j+} = C_{i,j+}\frac{p_{i,j} - p_{i,j+1}}{l}, \tag{58}$$

where p is the pressure. If the connection involves the fluid–fluid interface, the flow rate q is given by:

$$q_{i,j+} = C_{i,j+}\frac{\max(0, p_{i,j}^{\text{inv}} - p_{i,j+1}^{\text{def}} - p_{i,j+}^{\text{c}})}{l}, \tag{59}$$

Similarly, Eq. (58) and Eq. (59) can be written for $q_{i,j-}$, $q_{i-,j}$, and $q_{i+,j}$. The capillary pressure $p_{i,j+}^{\text{c}}$ (and similarly, $p_{i,j-}^{\text{c}}$, $p_{i-,j}^{\text{c}}$, and $p_{i+,j}^{\text{c}}$) is calculated based on

$$p^{\text{c}} = \gamma\Big(\frac{2\cos\theta}{h} + \frac{1}{r_2}\Big), \tag{60}$$

where γ is the interfacial tension, $h = 100\ \mu$m is the vertical gap, r_2 is the principal radii of curvature in the planar direction calculated based on the widths between posts, and θ is the equilibrium contact angle.

The conductance C is given by $C = \frac{kA}{\hat{\mu}}$, where $k = h^2/12$ is the permeability, $A = h\Delta x$ is the connection area, and $\hat{\mu}$ is a weighted average viscosity, which takes the value of μ_{inv}, μ_{def}, or $(\mu_{\text{inv}} + \mu_{\text{def}})/2$ depending on whether the connection is inside the invading phase, inside the defending phase, or at the fluid–fluid interface. When calculating the capillary pressure, we define the fluid–fluid interface at the connection between a fully invaded element and a non- or partially invaded element. This means we do not update the local interface location when an element is only partially invaded.

The volume conservation equation can be written for each element (i, j) by assuming incompressible fluids:

$$q_{i-,j} + q_{i+,j} + q_{i,j-} + q_{i,j+} = s_{i,j}, \tag{61}$$

where $s_{i,j}$ is a source term for the injection elements. Writing Eq. (61) for all elements gives a system of equations which need to be solved for pressure distribution given a certain set of boundary conditions. The nonlinear *max* function makes sovling the pressure directly from Eq. (61) impossible. Instead, we apply an iterative approach to obtain the pressure solution. The iterative solution of the volume conservation equation gives a pressure field, from which we explicitly compute the fluxes along the fluid–fluid interface using Eq. (59). At the start of each time step, the fraction of the volume occupied by the invading fluid $f_{i,j}$ at each element (i, j) is known. The time step Δt is calculated as the time required to completely fill one element at the interface. The invading fluid flows into all interface elements $(0 < f < 1)$ that have at least one connection with a positive flow rate, until one of the interface elements reaches $f = 1$. The change in volume fraction $\Delta f_{i,j}$ due to invasion at each time step is calculated as:

$$\Delta f_{i,j} = \frac{\Sigma q_{i,j}^{\text{interf}}\Delta t}{V}, \tag{62}$$

where $V = h\Delta x^2$ is the void volume of each element and $\Sigma q_{i,j}^{\text{interf}}$ represents the sum of the interfacial fluxes from the invading neighbours to the local defending element (i, j).

Numerical setup and boundary condition

The computational domain is discretized into a 1000×1000 grid with elements for the posts included but inactive for the simulations. Constant pressure of zero is imposed for elements with a distance from the center of injection larger than the radius of the micromodel. The simulated displacement patterns are shown in Figure S28.
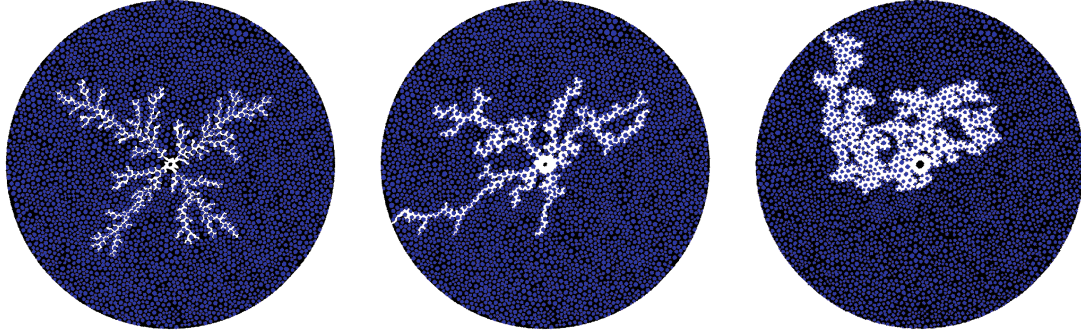

FIG. S28: Simulated displacement patterns for the strong drainage case at different injection rates (left to right: injection rate 0.2 mL/min, 0.02 ml/min, 0.002 ml/min).

Pore-network Model 5 (PN5)

Authors: Chao Yuan and Bruno Chareyre
Email: chao.yuan@3sr-grenoble.fr

Introduction

The model is based on a three-dimensional pore-network model named two-phase pore-scale finite volume discrete element method (2PFV-DEM) [38, 39]. It has been modified to tackle the geometry of this benchmark to simulate strong drainage at very small Ca. The void space is discretized in pore units with triangular prism geometry. The capillary entry pressure of each pore throat is determined by following the Mayer-Stowe-Princen (MS-P) method [94, 95]. Each pore is filled by only fluid phase; films and corner flows are not considered.
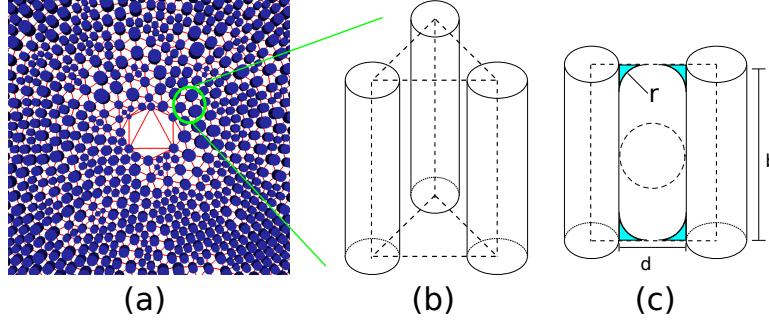

FIG. S29: Pore geometry. (a) A pore network created by the Regular Triangulation method. (b) A pore defined by a triangular prism. (c) Geometry of a pore throat.

Model Description

The void space between the posts is decomposed into large pore bodies connected by narrow throats via the Regular Triangulation method [96]. This method generalizes the classical Delaunay triangulation by including weighted points, where the weight accounts for the size of each post. A pore-scale network is established such that a triangular prism defines a pore and the common facet of two neighbouring pores defines a throat (Fig. S29).

The drainage of a single pore is determined by the relationship between local capillary pressure p^c and entry capillary pressure p_e^c of the throat. A pore is considered completely drained if $p^c > p_e^c$, such that each pore has only one state, either filled with wetting (W) phase or nonwetting (NW) phase.

The capillary entry pressure p_e^c of each throat is computed by following the Mayer-Stowe-Princen (MS-P) method, which employs the force balance on the multiple phases in a transient state [38]. The balance is written as:

$$\sum \vec{F}(p^c) = \vec{F}^c(p^c) + \vec{F}^t(p^c) = 0, \tag{63}$$

where $\vec{F}^c$ is the capillary force acting on the pore throat section, $\vec{F}^t$ is the total tension force along the contact line (see Fig. S29c). When $\sum \vec{F}(p^c) = 0$, p_e^c equals the value of p^c.

We assume the solid post is perfectly wetted by the defending fluid phase (*i.e.* $\theta = 180°$). The radius of the meniscus is denoted by $r \in [0, \min\{b, d\}]$, and the capillary pressure can be expressed by the Young-Laplace equation:

$$p^c = \frac{\gamma^{wn}}{r}. \tag{64}$$

$\vec{F}^c$ and $\vec{F}^t$ are written as follows,

$$\vec{F}^c = p^c A^{eff} = p^c(bd - 4r^2 + \pi r^2) \tag{65}$$

$$\vec{F}^t = \gamma^{wn} L_{wn} + \gamma^{ns} L_{ns} - \gamma^{ws} L_{ns} \tag{66}$$

where A^{eff} is the planar, projected area of the pore throat, L_{wn}, L_{ns} and L_{ws} are the contact line lengths between the multiple phases. The multiphase interfacial tensions, γ^{wn}, γ^{ns}, and γ^{ws} are related to θ via Young's equation:

$$\gamma^{\mathrm{ns}} - \gamma^{\mathrm{ws}} = \gamma^{\mathrm{wn}} \cos\theta \tag{67}$$

Combining Eqs. 63, 66, and 67, we arrive at the expression for $\vec{F}^{\mathrm{t}}$:

$$\vec{F}^{\mathrm{t}} = \gamma^{\mathrm{wn}}[2\pi r + 2(b + d - 4r)] \tag{68}$$

Combining Eqs. 64, 65, and 68, we arrive at the expression for p_e^{c}:

$$p_e^{\mathrm{c}} = \frac{\gamma^{\mathrm{wn}} * 2(4 - \pi)}{2(b + d) - \sqrt{4(b + d)^2 - 4(4 - \pi)bd}} \tag{69}$$

Overall, the drainage of the entire sample follows the invasion percolation model described by Chandler *et al.*, 1982 [97]. The simulation starts by increasing p^{c}. A search is then executed on the pore throats containing the fluid-fluid interface. The throat with the lowest p_e^{c} corresponds to the location where interface displacement will occur, leading to the invasion of a neighbouring pore by the NW phase. The NW phase reaches new throats when this pore is drained, which triggers a cascade of invasion events (*i.e.* Haines jumps) at pore throats with the same value of p^{c}. The invading phase thus percolates until no more pores can be drained.

In addition, the simulation is performed by controlling p^{c} instead of the flux rate. Although the model is designed for simulating quasi-static strong drainage, the effects of viscosity can be reflected by the rate of change of p^{c} (see Fig. S30).
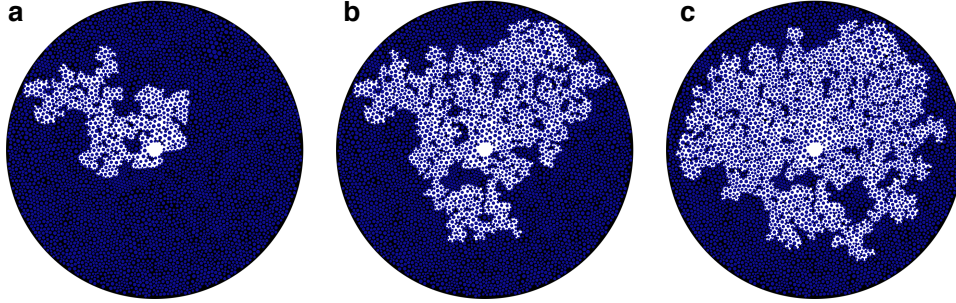

FIG. S30: Simulated displacement patterns for the strong drainage case for different rates of change of p^{c}. (a) p^{c} is increased from 0. The increment is locally determined by each throat, which corresponds to a purely quasi-static invasion sequence. In (b) and (c), p^{c} is decreased from the same initial value but with different declining speeds.